

Equivalence and Divergence of Bayesian Log-Odds and Dempster’s Combination Rule for 2D Occupancy Grids

Tatiana Berlenko¹ and Kirill Krinkin^{*1,2}

¹Constructor University, Bremen, Germany

²JetBrains LTD

Abstract

Prior comparisons of Dempster’s combination rule and Bayesian log-odds for occupancy grid mapping have not controlled for sensor model equivalence at the per-observation level, making it impossible to attribute observed performance differences to the fusion rule rather than to the sensor parameterization. We demonstrate that this methodological gap produces large confounds: in our own multi-robot experiment, unmatched parameterization reversed the boundary sharpness comparison from +12% in favor of belief functions to –22% in favor of Bayesian log-odds.

We introduce a pignistic-transform-based methodology that matches per-observation decision probabilities across frameworks, enabling controlled comparison of Bayesian log-odds, Dempster’s combination rule, and Yager’s rule in simulation (single-agent, multi-robot), across sensor parameters and clamping limits, and on two real indoor lidar datasets (Intel Research Lab, Freiburg Building 079). Real-data multi-robot conditions use scan-splitting with ideal alignment rather than true multi-robot deployment.

Under fair comparison with pignistic (BetP) matching, Bayesian fusion produces better point probabilities than Dempster’s rule: small absolute differences (0.001–0.022 on $[0, 1]$ scales across simulation and real data) are practically small. Bayesian log-odds is directionally favored in 15/15 per-metric simulation comparisons ($p = 3.1 \times 10^{-5}$); cell accuracy differences are additionally TOST-equivalent at nominal margins. Under normalized plausibility (P_{P1}) matching in single-agent simulation, the direction reverses: DS achieves better boundary sharpness (15/15) and Brier score (15/15), confirming that the comparison is matching-criterion-specific. An L_{\max} ablation confirms the Bayesian advantage under BetP matching arises from Dempster’s $1/(1 - K)$ conflict normalization, not from regularization. A downstream A* path-planning evaluation confirms functionally identical navigation outcomes. Previously reported Dempster–Shafer advantages may be attributable, at least in part, to unmatched sensor model parameterization.

The pignistic transform matching methodology is reusable for any future comparison of Bayesian and belief function fusion. These conclusions are restricted to point-probability metrics; the interval-valued representation $[\text{Bel}(A), \text{Pl}(A)]$ unique to belief functions is not evaluated here.

Keywords: occupancy grid mapping, Dempster–Shafer theory, Bayesian fusion, belief functions, pignistic transform, multi-sensor fusion, sensor model equivalence

1 Introduction

Occupancy grid mapping is a foundational capability in mobile robotics, providing a spatial representation that supports path planning, obstacle avoidance, and autonomous exploration. In

*Corresponding author: kirill@krinkin.com

the standard formulation, the environment is discretized into a regular grid of cells, each assigned a probability of being occupied based on accumulated sensor observations. This representation underpins widely deployed open-source Simultaneous Localization and Mapping (SLAM) systems including GMapping [Grisetti et al. \[2007\]](#), Google Cartographer [Hess et al. \[2016\]](#), and SLAM Toolbox [Macenski and Jambrecic \[2021\]](#), all of which use Bayesian log-odds fusion as the default grid update mechanism.

Two principled frameworks exist for fusing sensor observations into occupancy grid cells. The *Bayesian* approach, introduced by Elfes [Elfes \[1989\]](#) and refined by Thrun et al. [Thrun et al. \[2005\]](#), represents each cell’s state as a log-odds value that is incrementally updated with each observation. The approach is computationally efficient, mathematically transparent, and widely adopted. The *belief function* approach, grounded in Dempster–Shafer theory [Dempster \[1967\]](#), [Shafer \[1976\]](#) and its decision-theoretic extension, the Transferable Belief Model [Smets and Kennes \[1994\]](#), [Smets \[2005\]](#), represents each cell’s state as a mass function over the frame of discernment {occupied, free} and its power set. Belief function fusion has been applied to occupancy grids with reported advantages in dynamic environment detection through conflict analysis [Moras et al. \[2011b\]](#), SLAM with evidential reasoning [Huletski et al. \[2017\]](#), and random finite set formulations for dynamic occupancy grids [Nuss et al. \[2018\]](#). A comprehensive geometric treatment of the relationship between belief functions and probability distributions is provided by Cuzzolin [Cuzzolin \[2020\]](#).

Despite both frameworks being well-established, a controlled comparison that isolates the effect of the fusion rule from the sensor model parameterization has not been conducted. Prior studies comparing Bayesian and belief function occupancy grids have typically assigned sensor parameters independently for each framework: log-odds increments ($l_{\text{occ}}, l_{\text{free}}$) for the Bayesian arm and mass assignments (m_O, m_F, m_{OF}) for the belief function arm. When these parameters are not formally linked to produce equivalent per-observation decision probabilities, differences in the aggressiveness of the single-observation update can dominate the comparison, masking or even reversing the effect of the accumulation rule. This is a methodological gap, not an accusation of error: the sensor model equivalence problem was not previously recognized as a significant confound for occupancy grid comparisons.

In this paper, we set out to determine whether belief function fusion offers measurable advantages over Bayesian fusion for 2D occupancy grids when the comparison is controlled for sensor model equivalence. We develop a formal framework that connects the two representations, derive a fair comparison methodology, and validate the resulting comparison across simulation and real-data conditions. Our specific contributions are:

1. **Fair comparison methodology.** We develop a pignistic-transform-based methodology for matching Bayesian and belief function sensor models at the per-observation level, enabling controlled comparison of fusion rules independent of sensor parameterization. This methodology is reusable by the community for future comparisons (section 4).
2. **Combination rule mechanism analysis.** Through an L_{max} ablation ($L_{\text{max}} \in \{5, 10, 20, \infty\}$), a Yager’s rule comparison, and a DS regularization control ($m_{OF, \text{min}}$), we demonstrate that the Bayesian advantage persists when all regularization is removed ($L_{\text{max}} = \infty$) and cannot be closed by analogous DS regularization. This establishes the advantage as arising primarily from Dempster’s conflict normalization and the slower geometric convergence of belief masses at boundary cells, not a regularization artifact (section 7.1).
3. **Comprehensive empirical validation.** We compare four fusion rules (Bayesian, Bayesian with observation count, Dempster’s rule, Yager’s rule) across a sweep of L_{max} values, four sensor parameterizations, single-agent and multi-robot simulation, two real indoor lidar datasets (Intel Research Lab and Freiburg Building 079), and a downstream A* path-planning evaluation, demonstrating consistent Bayesian advantage under BetP matching across all simulation conditions (15/15 directional consistency per metric per condition)

and on both real datasets for cell accuracy and Brier score; under P_{P1} matching, the direction reverses (section 6.1.1). Boundary sharpness shows mixed results on Intel Lab, attributed to clamping artifacts confirmed by the L_{\max} ablation (section 6).

We restrict our analysis to 2D binary occupancy grids with lidar-type sensors. The theoretical results (Equivalence Theorem, m_{OF} decay proof) are dimension-independent, but the experimental validation is restricted to 2D indoor environments. We test two combination rules (Dempster’s rule and Yager’s rule) to isolate the role of conflict normalization; extension to 3D grids, multi-hypothesis frames, and additional combination rules (PCR6, Dubois–Prade) is discussed as future work.

Sections 2 and 3 review background and present the theoretical analysis. Section 4 develops the fair comparison methodology. Sections 5 and 6 describe the experimental setup and results. Section 7 discusses mechanisms and practical recommendations. Section 8 summarizes conclusions and future directions.

2 Related Work

Occupancy grid mapping has been approached from two complementary theoretical perspectives: Bayesian probability theory and Dempster–Shafer belief function theory. This section reviews the key developments in each line of work and identifies a methodological gap in prior comparison studies that motivates the present investigation.

2.1 Bayesian Occupancy Grid Mapping

Elfes [Elfes \[1989\]](#) introduced the occupancy grid as a spatial representation for mobile robot perception, in which each cell stores an independent occupancy probability updated from sensor observations via Bayes’ rule. Thrun et al. [Thrun et al. \[2005\]](#) systematised the approach within the broader framework of probabilistic robotics, introducing the log-odds representation $L = \log(p/(1 - p))$ that converts multiplicative Bayesian updates into efficient additive operations. This formulation, combined with clamping of accumulated log-odds to a symmetric bound $|L| \leq L_{\max}$ for numerical stability, has become the standard implementation in the robotics community.

The Bayesian log-odds approach is the default in widely deployed open-source SLAM systems, including GMapping [Grisetti et al. \[2007\]](#) (Rao-Blackwellised particle filter SLAM), Google Cartographer [Hess et al. \[2016\]](#) (submap-based graph SLAM), and SLAM Toolbox [Macenski and Jambrecic \[2021\]](#) (the Robot Operating System (ROS) 2 navigation stack default). Its popularity rests on simplicity (one floating-point value per cell), computational efficiency (one addition per update), and the well-understood Bayesian interpretation of the resulting probabilities. The formal treatment of Bayesian occupancy grid fusion is given in Section 3.1.

2.2 Belief Function Occupancy Grid Mapping

An alternative line of work applies Dempster–Shafer (DS) belief function theory [Dempster \[1967, 1968\]](#), [Shafer \[1976\]](#) to occupancy grid mapping, replacing the single occupancy probability with a basic belief assignment (BBA) that explicitly represents ignorance. Within the Transferable Belief Model (TBM) [Smets and Kennes \[1994\]](#), each cell stores a mass triplet (m_O, m_F, m_{OF}) where m_{OF} quantifies the degree of epistemic ignorance—mass not yet committed to either hypothesis. Decisions are made via the pignistic transform [Smets \[2005\]](#): the pignistic probability of occupancy is $\text{BetP}(O) = m_O + m_{OF}/2$, mapping belief functions to probabilities for action selection. Cuzzolin [Cuzzolin \[2020\]](#) provides a modern geometric treatment of the relationship between belief functions and probability, situating the pignistic transform within a broader family of probability transforms on the belief space.

Moras et al. [Moras et al. \[2011b,a\]](#) developed *credibilist occupancy grids* for vehicle perception in dynamic traffic environments, proposing the use of conflict mass K between successive observations as a metric for detecting moving objects. Their approach demonstrated that cells affected by dynamic obstacles produce elevated conflict under Dempster’s combination rule, providing a mechanism for dynamic detection that has no direct analogue in standard Bayesian grids.

Huletski et al. [Huletski et al. \[2017\]](#) presented vinySLAM, an indoor SLAM system that replaces the single-probability cell model of tinySLAM with TBM-based mass triplets, targeting resource-constrained platforms such as the Raspberry Pi. The system demonstrated accuracy improvements over tinySLAM on indoor benchmarks. However, vinySLAM simultaneously modified both the occupancy cell model (from Bayesian to TBM) and the scan matching cost function (adding angle-histogram-based weighting). No ablation study has been published that isolates the contribution of the TBM cell model from the improved scan matching, leaving the source of the accuracy improvement ambiguous (disclosure: the second author of the present work is a co-author of [Huletski et al. \[2017\]](#)).

Nuss et al. [Nuss et al. \[2018\]](#) proposed a random finite set (RFS) approach to occupancy grids that provides a principled treatment of multi-target tracking within the belief function framework, extending evidential occupancy modelling to dynamic multi-object scenarios. Richter et al. [Richter et al. \[2021\]](#) extended evidential grids to semantic occupancy mapping for outdoor environments using monocular and stereo cameras. Ben Ayed et al. [Ben Ayed et al. \[2025\]](#) provide a recent survey of evidential occupancy grid methods and their extensions.

Several advantages of the belief function approach have been reported in this literature:

1. **Dynamic object detection:** conflict analysis under Dempster’s rule can identify cells with inconsistent temporal observations [Moras et al. \[2011b\]](#).
2. **Richer uncertainty representation:** the ignorance mass m_{OF} distinguishes cells that are unobserved (high m_{OF}) from cells with balanced conflicting evidence (low m_{OF} , similar m_O and m_F), a distinction that a single probability cannot express [Smets and Kennes \[1994\]](#).
3. **Interval-valued bounds:** the belief–plausibility interval $[\text{Bel}(O), \text{Pl}(O)]$ provides conservative decision bounds that may be useful for guaranteed-safe path planning.

These advantages are theoretically well-motivated. The question addressed by the present work is whether they translate to measurable performance gains under a controlled comparison with matched sensor model parameterization.

Alternative combination rules Dempster’s rule is one of several operators for combining belief functions. Its conflict normalization by $1/(1-K)$ has been the subject of long-standing discussion since Zadeh’s [Zadeh \[1979\]](#) observation that normalization can produce counterintuitive results under high conflict. Alternative rules address this differently: Yager’s rule [Yager \[1987\]](#) assigns conflict mass to total ignorance m_{OF} ; the Dubois–Prade rule [Dubois and Prade \[1988\]](#) redistributes conflict to the union of focal elements; Denoeux’s cautious rule [Denoeux \[2008\]](#) provides a least-committed combination for non-distinct evidence; PCR (proportional conflict redistribution) distributes conflict mass proportionally among contributing hypotheses [Smarandache and Dezert \[2006\]](#), [Moras et al. \[2015\]](#); distributed combination for multi-robot scenarios has been addressed in [Denoeux \[2021\]](#). Our analysis is specific to Dempster’s rule, which is the canonical DS combination operator and the most widely used in the evidential occupancy grid literature [Moras et al. \[2011b,a\]](#), [Huletski et al. \[2017\]](#). Whether the findings reported here generalize to alternative rules is a question for future work. In particular, the clamping asymmetry mechanism identified in Section 4.4 depends on Dempster’s conflict normalization; rules that handle conflict differently may not exhibit this behavior.

2.3 Comparison Studies and the Sensor Model Gap

Despite the growing body of work on belief function occupancy grids, controlled comparisons between the two frameworks remain scarce, and those that exist share a common methodological limitation: sensor model parameters are chosen independently for each framework. In the credibilist grid literature [Moras et al. \[2011b,a\]](#), Bayesian log-odds and belief function masses are set separately; in vinySLAM [Huletski et al. \[2017\]](#), the TBM cell model and scan matching cost function were changed simultaneously without ablation; the RFS-based approach [Nuss et al. \[2018\]](#) uses observation models specific to the RFS framework. In all cases, the absence of a formal matching criterion means that observed performance differences reflect an unknown mixture of sensor model and fusion rule effects (detailed critique in Supplementary Material).

The methodological gap To our knowledge, no prior comparison of Bayesian and belief function occupancy grid fusion has applied per-observation sensor model matching via the pignistic transform. This matching—requiring that the pignistic probability $\text{BetP}(O)$ equal the Bayesian posterior $\sigma(l)$ for each individual sensor observation—ensures that any aggregate performance difference is attributable to the multi-observation accumulation rule (additive log-odds with clamping versus Dempster’s combination with conflict normalization), not to the single-observation sensor model. This methodology is developed in Section 4 and constitutes one of the main contributions of the present work.

We emphasize that the absence of per-observation matching in prior work is a previously unrecognized methodological confound, not an error by prior authors. The belief function and Bayesian communities have traditionally parameterized their sensor models according to framework-specific conventions, and there has been no established procedure for cross-framework matching. The pignistic transform provides a natural and principled bridge, but its application to sensor model matching for controlled comparisons appears to be novel. Customizable frameworks for evidential occupancy grids have been proposed [Porebski \[2020\]](#), but per-observation matching between Bayesian and belief function sensor models has not been addressed.

3 Theoretical Foundations

This section establishes two formal results that hold independently of the experimental evaluation presented in Section 6. Theorem 3.2 proves that the Bayesian log-odds and belief function representations encode identical decision probabilities at the single-observation level, formalizing a connection long recognized informally in both communities. Theorem 3.5 proves that the ignorance mass m_{OF} decreases strictly under any informative observation, constraining the utility of its raw magnitude as a standalone dynamic detection metric.

3.1 Bayesian Occupancy Grid Fusion

Each cell in a Bayesian occupancy grid maintains a log-odds value

$$L = \log \frac{p}{1-p}, \quad (1)$$

where $p = P(O)$ denotes the occupancy probability [Elfes \[1989\]](#). The inverse relationship is $p = \sigma(L) \triangleq (1 + e^{-L})^{-1}$.

Given a sensor observation with log-odds increment l_{occ} (for occupied cells) or l_{free} (for free-space cells), the Bayesian update is additive in log-odds:

$$L_{k+1} = L_k + l_{\text{obs}}, \quad (2)$$

where $l_{\text{obs}} \in \{l_{\text{occ}}, l_{\text{free}}\}$ depends on the cell classification produced by the inverse sensor model. Since the update is additive, the result is independent of observation order.

To prevent numerical overflow and excessive confidence, accumulated values are clamped to a symmetric range:

$$L \leftarrow \text{clamp}(L, -L_{\max}, L_{\max}), \quad (3)$$

with $L_{\max} = 10$ being a common default, corresponding to a maximum probability $p_{\max} = \sigma(10) \approx 0.999955$.

A count-augmented representation (L, n) tracks the number of observations n alongside the accumulated log-odds, providing a measure of evidential support that is not encoded by L alone.

3.2 Dempster–Shafer Belief Function Fusion

For binary occupancy, the frame of discernment is $\Theta = \{O, F\}$ (occupied, free) with power set $2^\Theta = \{\{O\}, \{F\}, \Theta\}$. A basic belief assignment (BBA) is a function $m: 2^\Theta \rightarrow [0, 1]$ with $m(\emptyset) = 0$ and $\sum_{A \subseteq \Theta} m(A) = 1$ [Shafer \[1976\]](#). We write (m_O, m_F, m_{OF}) for $(m(\{O\}), m(\{F\}), m(\Theta))$, so that $m_O + m_F + m_{OF} = 1$.

Dempster’s combination rule [Dempster \[1967, 1968\]](#) fuses two independent BBAs m_1, m_2 as:

$$m_{12}(C) = \frac{1}{1 - K} \sum_{\substack{A \cap B = C \\ A, B \subseteq \Theta}} m_1(A) m_2(B), \quad C \neq \emptyset, \quad (4)$$

where the conflict mass (specialised here to the binary frame, where the only empty-intersection pairs are $\{O\} \cap \{F\}$ and $\{F\} \cap \{O\}$) is

$$K = \sum_{A \cap B = \emptyset} m_1(A) m_2(B) = m_O^{(1)} m_F^{(2)} + m_F^{(1)} m_O^{(2)}. \quad (5)$$

For the binary frame, the combined masses expand to:

$$m_O^{(12)} = \frac{m_O^{(1)} m_O^{(2)} + m_O^{(1)} m_{OF}^{(2)} + m_{OF}^{(1)} m_O^{(2)}}{1 - K}, \quad (6)$$

$$m_F^{(12)} = \frac{m_F^{(1)} m_F^{(2)} + m_F^{(1)} m_{OF}^{(2)} + m_{OF}^{(1)} m_F^{(2)}}{1 - K}, \quad (7)$$

$$m_{OF}^{(12)} = \frac{m_{OF}^{(1)} m_{OF}^{(2)}}{1 - K}. \quad (8)$$

To derive a decision probability from a BBA, the pignistic transform [Smets \[2005\]](#) distributes the ignorance mass m_{OF} equally between singletons, following the principle of insufficient reason within the Transferable Belief Model (TBM) [Smets and Kennes \[1994\]](#):

$$\text{BetP}(O) = m_O + \frac{1}{2} m_{OF}. \quad (9)$$

Remark 3.1 (Consonant mass functions). A single-source sensor observation produces a *consonant* BBA in which mass is assigned to either $\{O\}$ or $\{F\}$ but never both simultaneously, so that $m_O \cdot m_F = 0$. The focal elements are therefore nested ($\{O\} \subset \Theta$ or $\{F\} \subset \Theta$), which is the defining property of consonance. This constraint holds throughout sequential accumulation from a vacuous prior when all observations agree in sign, but is violated after the first pair of conflicting observations (one occupied, one free), which produces $m_O > 0$ and $m_F > 0$ simultaneously. Since boundary cells—where the Bayesian/DS comparison matters most—receive conflicting observations by definition, they operate in the non-consonant regime after the first few updates.

3.3 Equivalence Theorem

We now establish a bijection between the Bayesian log-odds and belief function representations at the single-observation level. This result formalizes the observation, recognized informally in the belief function community, that Dempster–Shafer theory on the binary frame $\{O, F\}$ yields identical *decision probabilities* to the Bayesian model for a single consonant observation [Smets and Kennes \[1994\]](#). The equivalence is at the decision level via BetP; the TBM retains a richer representation (the mass triplet) even when the decision probability matches. The bijection follows from the BBA constraint structure on binary frames and is implicit in the literature; the contribution here is its explicit construction and application to sensor model matching for controlled fusion comparison.

Theorem 3.2 (Single-observation equivalence). *Define the mapping $\varphi: \mathbb{R} \rightarrow \mathcal{M}$, where \mathcal{M} denotes the set of consonant BBAs on $\{O, F\}$ with $m_{OF} > 0$, from log-odds values by:*

$$\varphi(L) = \begin{cases} m_O = 2\sigma(L) - 1, & m_F = 0, & m_{OF} = 2(1 - \sigma(L)) & \text{if } L \geq 0, \\ m_O = 0, & m_F = 1 - 2\sigma(L), & m_{OF} = 2\sigma(L) & \text{if } L < 0, \end{cases} \quad (10)$$

where $\sigma(L) = (1 + e^{-L})^{-1}$. Then:

- (i) $\varphi(L)$ is a valid BBA: all components are non-negative and sum to 1.
- (ii) The pignistic probability reproduces the Bayesian occupancy probability exactly: $\text{BetP}(O) = \sigma(L)$.
- (iii) φ is a bijection between \mathbb{R} and the set of consonant BBAs on $\{O, F\}$ with $m_{OF} > 0$.

Proof. (i) For $L \geq 0$, we have $\sigma(L) \in [\frac{1}{2}, 1)$, so $m_O = 2\sigma(L) - 1 \in [0, 1)$, $m_F = 0$, and $m_{OF} = 2(1 - \sigma(L)) \in (0, 1]$. The sum is $m_O + m_F + m_{OF} = (2\sigma(L) - 1) + 0 + 2 - 2\sigma(L) = 1$. The case $L < 0$ is symmetric with $\sigma(L) \in (0, \frac{1}{2}]$.

(ii) For $L \geq 0$:

$$\text{BetP}(O) = m_O + \frac{1}{2} m_{OF} = (2\sigma(L) - 1) + (1 - \sigma(L)) = \sigma(L).$$

For $L < 0$: $\text{BetP}(O) = 0 + \frac{1}{2} \cdot 2\sigma(L) = \sigma(L)$.

(iii) The inverse mapping is $\varphi^{-1}(m) = \log \frac{\text{BetP}(O)}{1 - \text{BetP}(O)}$, where $\text{BetP}(O) = m_O + m_{OF}/2$. Since σ is a bijection from \mathbb{R} onto $(0, 1)$ and $\text{BetP}(O) \in (0, 1)$ for any consonant BBA with $m_{OF} > 0$, the composition is bijective. The consonance constraint and $m_{OF} > 0$ are preserved by construction: $m_O \cdot m_F = 0$ holds in both cases, and $m_{OF} = 2 \min(\sigma(L), 1 - \sigma(L)) > 0$ for all $L \in \mathbb{R}$. \square

Corollary 3.3 (Single-observation equivalence). *For a single sensor observation, applying the Bayesian update from prior $L_0 = 0$ with increment l_{obs} and applying Dempster’s combination from the vacuous prior $m = (0, 0, 1)$ with observation $\varphi(l_{\text{obs}})$ produce identical decision probabilities: $\sigma(l_{\text{obs}}) = \text{BetP}(O)$.*

Proof. The vacuous prior acts as the identity element for Dempster’s rule, so one application of (4) returns the observation BBA $\varphi(l_{\text{obs}})$ unchanged. By Theorem 3.2 (ii), its pignistic probability equals $\sigma(l_{\text{obs}})$, which is also the Bayesian posterior from $L_0 = 0$. \square

Lemma 3.4 (Closed-form accumulation under consonant observations). *Starting from the vacuous prior $m = (0, 0, 1)$, after N_{obs} identical consonant occupied observations with $m_{\text{obs}} = (a, 0, 1 - a)$ where $0 < a < 1$, Dempster’s rule yields:*

$$m_O^{(N_{\text{obs}})} = 1 - (1 - a)^{N_{\text{obs}}}, \quad m_F^{(N_{\text{obs}})} = 0, \quad m_{OF}^{(N_{\text{obs}})} = (1 - a)^{N_{\text{obs}}}. \quad (11)$$

The symmetric result holds for free observations.

The proof is by induction on N (Supplementary Material, Section S2). This closed form applies to the zero-conflict case ($K = 0$); boundary cells with mixed observations require numerical evaluation.

The equivalence of Theorem 3.2 holds at the single-observation level. Under repeated observations, the two mechanisms diverge due to (a) the Bayesian clamp imposing an artificial ceiling and (b) Dempster’s $1/(1 - K)$ conflict normalization having no Bayesian analogue. Quantitative analysis is in Section 4.4.

3.4 Monotonic Decay of m_{OF}

The ignorance mass m_{OF} has been proposed as a metric for detecting dynamic objects in evidential occupancy grids, on the hypothesis that cells affected by moving objects would maintain elevated m_{OF} due to conflicting observations. The following theorem shows that m_{OF} decreases strictly under *any* informative observation, regardless of the observation content.

Theorem 3.5 (Monotonic decay of m_{OF}). *Let $m^{\text{pr}} = (m_O^{\text{pr}}, m_F^{\text{pr}}, m_{OF}^{\text{pr}})$ be a prior BBA with $m_{OF}^{\text{pr}} > 0$, and let $m^{\text{obs}} = (m_O^{\text{obs}}, m_F^{\text{obs}}, m_{OF}^{\text{obs}})$ be a non-degenerate observation, meaning $0 < m_{OF}^{\text{obs}} < 1$. Then the posterior ignorance mass after Dempster combination satisfies*

$$m_{OF}^{\text{post}} < m_{OF}^{\text{pr}}. \quad (12)$$

Proof. From (8), the posterior ignorance mass is

$$m_{OF}^{\text{post}} = \frac{m_{OF}^{\text{pr}} \cdot m_{OF}^{\text{obs}}}{1 - K}, \quad (13)$$

where $K = m_O^{\text{pr}} m_F^{\text{obs}} + m_F^{\text{pr}} m_O^{\text{obs}} \geq 0$. Note that $K < 1$ is guaranteed since $m_{OF}^{\text{pr}} > 0$ and $m_{OF}^{\text{obs}} > 0$. It suffices to show $m_{OF}^{\text{obs}} < 1 - K$, since this yields $m_{OF}^{\text{obs}}/(1 - K) < 1$ and hence (12). Substituting $m_{OF}^{\text{obs}} = 1 - m_O^{\text{obs}} - m_F^{\text{obs}}$:

$$\begin{aligned} 1 - K - m_{OF}^{\text{obs}} &= 1 - m_O^{\text{pr}} m_F^{\text{obs}} - m_F^{\text{pr}} m_O^{\text{obs}} - 1 + m_O^{\text{obs}} + m_F^{\text{obs}} \\ &= m_O^{\text{obs}} \underbrace{(1 - m_F^{\text{pr}})}_{= m_O^{\text{pr}} + m_{OF}^{\text{pr}}} + m_F^{\text{obs}} \underbrace{(1 - m_O^{\text{pr}})}_{= m_F^{\text{pr}} + m_{OF}^{\text{pr}}}. \end{aligned} \quad (14)$$

Since the observation is non-degenerate ($m_{OF}^{\text{obs}} < 1$), at least one of m_O^{obs} or m_F^{obs} is strictly positive. Since $m_{OF}^{\text{pr}} > 0$, both coefficients $(m_O^{\text{pr}} + m_{OF}^{\text{pr}})$ and $(m_F^{\text{pr}} + m_{OF}^{\text{pr}})$ are strictly positive. Therefore the right-hand side of (14) is strictly positive, giving $m_{OF}^{\text{obs}} < 1 - K$ and hence $m_{OF}^{\text{post}} < m_{OF}^{\text{pr}}$. \square

Corollary 3.6 (Exponential decay under consonant observations). *Under the conditions of Theorem 3.4, the ignorance mass decays exponentially: $m_{OF}^{(N_{\text{obs}})} = (1 - a)^{N_{\text{obs}}}$, so that $m_{OF}^{(N_{\text{obs}})} \rightarrow 0$ as $N_{\text{obs}} \rightarrow \infty$ for any $a \in (0, 1)$.*

Remark 3.7 (Scope of Theorem 3.5). The raw magnitude of m_{OF} cannot serve as a standalone dynamic detection metric, as it decreases monotonically regardless of environment dynamics. However, derived quantities—the rate of change $\Delta m_{OF}^{(k)}$, the pignistic uncertainty $u_{\text{pign}} = 1 - |2 \text{BetP}(O) - 1|$, or the full TBM state—could in principle detect dynamics through mass redistribution under conflicting observations. Whether these capabilities translate to practical advantages is an empirical question addressed in Section 6.

4 Fair Comparison Methodology

Armed with the formal equivalence results of section 3—in particular, the bijection φ between log-odds and consonant belief masses—we now develop the fair comparison methodology that operationalises this bijection for experimental use.

A meaningful comparison of Bayesian and belief function fusion requires that any observed performance difference be attributable to the fusion rule itself, not to differences in per-observation sensor model parameterization. This section develops a *decision-theoretic* methodology based on the pignistic transform that ensures per-observation equivalence at the decision level, analyzes its locality properties, and characterizes the divergence mechanism that arises under multi-observation accumulation. The matching is decision-theoretic rather than representationally neutral: it equates pignistic probabilities, not the belief function representations themselves. Alternative probability transforms (plausibility, maximum entropy) would yield different matched masses and thus a different comparison.

4.1 The Sensor Model Equivalence Problem

In an initial multi-robot experiment (three robots, dynamic obstacles, 15 independent runs), belief function fusion achieved +12% higher boundary sharpness than Bayesian fusion. After applying the pignistic transform matching procedure described below—which constrains the belief function masses to produce identical per-observation decision probabilities—the same experiment yielded a −22% to −29% boundary sharpness *deficit* for belief function fusion (−22% under the dynamic-baseline condition, −29% under elevated sensor noise), with 15/15 directional consistency favoring the Bayesian arm. The reversal was caused entirely by the sensor model parameterization, not by any change to the fusion algorithms themselves. This motivates a formal matching criterion: the per-observation update must produce *identical decision probabilities* under both frameworks before any multi-observation accumulation occurs.

4.2 Pignistic Transform Matching

We derive matched belief function masses from Bayesian log-odds parameters using the pignistic probability transform Smets [2005]. Given a basic belief assignment m on the binary frame $\Theta = \{O, F\}$, the pignistic probability of occupancy is

$$\text{BetP}(O) = m_O + \frac{m_{OF}}{2}$$

(restated from eq. (9) for reader convenience).

In the Bayesian framework, a single observation with log-odds l produces the occupancy probability $p = \sigma(l)$, where $\sigma(l) = 1/(1 + e^{-l})$ is the logistic sigmoid. The matched masses derived below are the constructive application of the bijection φ from Theorem 3.2: given l , the unique consonant BBA satisfying $\text{BetP}(O) = \sigma(l)$ is precisely $\varphi(l)$. We restate the construction explicitly for reader convenience. The matching condition requires

$$\text{BetP}(O) = \sigma(l), \tag{15}$$

for each observation type (occupied hit or free traversal).

Setting $p = \sigma(l)$ and requiring that $m_O + m_F + m_{OF} = 1$ with all masses non-negative, the unique solution is:

$$m_O = \max(0, 2p - 1), \tag{16}$$

$$m_F = \max(0, 1 - 2p), \tag{17}$$

$$m_{OF} = 1 - |2p - 1|. \tag{18}$$

Verification is immediate: $m_O + m_{OF}/2 = \max(0, 2p - 1) + (1 - |2p - 1|)/2 = p$ for both $p \geq 0.5$ and $p < 0.5$.

Numerical example For the sensor parameters used in all experiments ($l_{\text{occ}} = 2.0$, $l_{\text{free}} = -0.5$):

- **Occupied hit:** $p = \sigma(2.0) = 0.8808$; $m = (0.7616, 0, 0.2384)$; $\text{BetP}(O) = 0.7616 + 0.2384/2 = 0.8808$.
- **Free traversal:** $p = \sigma(-0.5) = 0.3775$; $m = (0, 0.2449, 0.7551)$; $\text{BetP}(O) = 0 + 0.7551/2 = 0.3775$.

In both cases, the pignistic probability equals the Bayesian probability exactly.

Choice of probability transform We adopt BetP because it is the standard decision-theoretic bridge within the TBM Smets [2005] and the most widely used in the evidential occupancy grid literature Moras et al. [2011b], Huletski et al. [2017]. The matching is BetP-specific; the normalized plausibility transform $P_{\text{Pl}}(O) = \text{Pl}(O)/(\text{Pl}(O) + \text{Pl}(F))$ yields different matched masses. For $l_{\text{occ}} = 2.0$ ($p = 0.8808$): BetP matching gives $m = (0.762, 0, 0.238)$, while P_{Pl} matching gives $m = (0.865, 0, 0.135)$ —44% less ignorance mass per observation, producing sharper DS updates. Under multi-observation accumulation the combined BBA becomes non-consonant at boundary cells (where both $m_O > 0$ and $m_F > 0$), and BetP and normalized plausibility diverge further; our evaluation is therefore BetP-specific throughout, with single-agent P_{Pl} sensitivity analysis reported in section 6.1.

Terminology “Dempster’s rule” denotes the normalized combination rule ($1/(1 - K)$ conflict normalization); “DS” is used as shorthand in tables and figures.

Consonant mass functions The pignistic-derived masses are consonant ($m_F = 0$ for occupied, $m_O = 0$ for free observations), reflecting the physical constraint of single-source inverse sensor models: a lidar beam returns evidence for *either* occupancy or free space, never both simultaneously. All prior DS occupancy grid work cited here Moras et al. [2011b,a], Huletski et al. [2017] uses consonant BBAs for the same reason. Non-consonant BBAs from multi-source fusion fall outside this scope.

4.3 Per-Observation Locality

A critical property of the pignistic matching is that it holds *per-observation*: at each specific sensor distance d and angle of incidence α , the matching condition (15) is satisfied independently.

In the single-agent simulation experiment (section 5.1.1), the sensor model is non-homogeneous: log-odds values decay exponentially with distance and angle of incidence,

$$l(d, \alpha) = l_{\text{obs}} \cdot \exp(-\lambda_d d) \cdot \exp(-\lambda_\alpha \alpha), \quad (19)$$

where $l_{\text{obs}} \in \{l_{\text{occ}}, l_{\text{free}}\}$ and $(\lambda_d, \lambda_\alpha) = (0.1, 0.5)$ are the distance and angle decay rates respectively. Because the pignistic-derived masses are computed from $p = \sigma(l(d, \alpha))$ at each (d, α) pair individually, the matching holds at every observation regardless of the spatial variation in sensor confidence. The Equivalence Theorem (section 3.3) therefore applies locally to each per-observation update, even though the global sensor model is non-homogeneous.

This per-observation locality is the key property that enables fair comparison under realistic sensor models. It ensures that any aggregate performance difference between the two frameworks must arise from the multi-observation *accumulation rule*—Bayesian log-odds addition with clamping versus Dempster’s combination with conflict normalization—not from the single-observation updates.

The multi-robot simulation, mechanism test, and real-data (scan-split) experiments use constant sensor parameters ($l_{\text{occ}} = 2.0$, $l_{\text{free}} = -0.5$) with pignistic-matched constant masses. The

per-observation locality argument still holds—it simply reduces to a single matching point rather than a continuous function of (d, α) . The non-homogeneous model is exercised only in the single-agent experiment to demonstrate that the methodology extends to spatially varying sensor confidence; the real-data sensor model is not calibrated to the SICK LMS200 specifically. Although the sensor parameter sensitivity analysis (Supplementary Material, Section S4) confirms the Bayesian advantage across four parameterizations in simulation, the real-data experiments use only the default parameterization; real-data sensitivity to sensor parameters remains untested.

4.4 Clamping Asymmetry Analysis

Although per-observation updates are identical by construction, the two frameworks accumulate evidence differently over multiple observations. We analyze this divergence for the parameters used in our experiments ($l_{\text{occ}} = 2.0$, clamp limit $L_{\text{max}} = 10$).

Bayesian accumulation The log-odds accumulator clamps at $|L| \leq L_{\text{max}}$:

$$L^{(N)} = \min(L^{(0)} + N \cdot l_{\text{occ}}, L_{\text{max}}). \quad (20)$$

For $l_{\text{occ}} = 2.0$ and $L^{(0)} = 0$, the clamp saturates at $N = 5$, yielding $p(O) = \sigma(10) = 0.999955$ permanently.

Dempster–Shafer accumulation Starting from the vacuous prior $m = (0, 0, 1)$ and applying N identical occupied observations with $m_{\text{obs}} = (a, 0, 1 - a)$ where $a = 0.7616$, Dempster’s combination produces (by induction; see section 3.3):

$$m_O^{(N)} = 1 - (1 - a)^N, \quad m_{OF}^{(N)} = (1 - a)^N, \quad \text{BetP}(O) = 1 - \frac{(1 - a)^N}{2}. \quad (21)$$

Since all observations agree ($m_{F,\text{obs}} = 0$), there is no conflict ($K = 0$), and $\text{BetP}(O)$ converges asymptotically to 1.0 with no artificial ceiling.

The convergence trajectories are compared in Supplementary Material, Section S3: the methods agree at $N = 1$ (by construction), Bayesian leads at $N = 2$ –5, clamps at $N = 5$, and is overtaken by Dempster–Shafer at approximately $N = 7$.

Two divergence mechanisms For interior cells ($N \gg 5$, consistent observations), Dempster–Shafer produces marginally higher confidence ($\text{BetP} \rightarrow 1.0$ vs. $p = 0.999955$), a difference that does not affect classification. For boundary cells with conflicting observations, Dempster’s multiplicative combination with $1/(1 - K)$ normalization converges more slowly to certainty than additive log-odds—e.g., after 5 occupied and 5 free observations, $\text{BetP}(O) = 0.9973$ vs. $p(O) = 0.9994$. The net aggregate effect favors Bayesian fusion because boundary cells are where classification errors concentrate.

5 Experimental Setup

We evaluate the two fusion frameworks across three conditions: a controlled single-agent simulation, a multi-robot simulation with pose graph optimization, and real-data validation on two standard indoor lidar datasets.

5.1 Simulation Environments

5.1.1 Single-Agent Comparison

The single-agent experiment uses procedurally generated 2D environments of 50×50 m at 0.1 m grid resolution (500×500 cells). Each environment contains 3 rooms connected by 4 corridors,

5 static obstacles (convex polygons), and 3 dynamic obstacles moving at 0.5 m/s. A single robot follows a deterministic counter-clockwise perimeter patrol trajectory (step size ≈ 0.38 m) with a simulated lidar sensor: 180 rays, 360° field of view (2° angular spacing), 15 m maximum range, Gaussian range noise $\sigma_r = 0.02$ m.

The sensor model is non-homogeneous (section 4.3), with base parameters $l_{\text{occ}} = 2.0$, $l_{\text{free}} = -0.5$ and decay rates $\lambda_d = 0.1$, $\lambda_\alpha = 0.5$. The belief function arm uses pignistic-matched masses derived from these log-odds at each (d, α) pair. The Bayesian arm clamps at $L_{\text{max}} = 10$. Each condition is repeated for 15 independent runs with seeds 42–56.

5.1.2 Multi-Robot Comparison

The multi-robot experiment uses 20×20 m environments at 0.1 m resolution (200×200 cells) with 1 room, 5 static obstacles, and 3 dynamic obstacles (speed 0.3 m/s). Three robots explore simultaneously, each following a counter-clockwise perimeter patrol trajectory (200 steps, step size ≈ 0.36 m) with 90-ray lidar (360° field of view, 4° angular spacing, 8 m range, $\sigma_r = 0.03$ m). Odometry drift is simulated with $\sigma_{\text{trans}} = 0.02$ m and $\sigma_{\text{rot}} = 0.005$ rad per step. Robots start at different positions along the environment perimeter.

Individual robot maps are aligned via pose graph optimization (PGO) triggered by rendezvous detection at 2.5 m proximity, then fused cell-wise. Two conditions are tested: a *dynamic baseline* (nominal noise) and a *noisy sensor* condition (elevated sensor noise). Each condition uses 15 independent runs.

Simulation scope Simulation environments are geometrically simpler than real-world datasets (fewer obstacles, convex geometries). Real-data validation (section 5.2) confirms generalization to complex indoor geometries.

5.2 Real Data: Intel Lab and Freiburg 079

5.2.1 Intel Research Lab

The Intel Research Lab dataset [Haehnel \[2003\]](#) contains laser scans collected by a mobile robot in an office environment with furniture, narrow passages, and non-convex obstacles. The sensor is a SICK LMS200 lidar with 180 beams and 180° field of view. We set the effective maximum range to 8.0 m, discarding returns beyond this threshold to match the indoor operating regime.

Scans are split 80%/20% into training and test sets. The training set is used for map construction (both Bayesian and belief function arms process identical scan sequences); the test set generates ground truth occupancy labels for evaluation. This train/test split ensures that ground truth is independent of the mapping data, avoiding circular evaluation.

Scan-split fusion conditions are created by splitting the training scans into $R \in \{2, 4\}$ interleaved subsequences, each assigned to a separate virtual robot. Individual maps are constructed independently and then fused cell-wise, identical to the simulation multi-robot protocol. Real-data scan-split conditions test sensitivity to data partitioning under ideal alignment, not end-to-end multi-robot SLAM performance. This procedure eliminates alignment uncertainty and coverage heterogeneity present in true multi-robot deployments.

Sensor parameters ($l_{\text{occ}} = 2.0$, $l_{\text{free}} = -0.5$) are identical to the simulation experiments; belief function masses are derived via the pignistic transform at each observation.

5.2.2 Freiburg Building 079

The Freiburg 079 dataset provides laser scans from a Pioneer 2 robot equipped with a SICK LMS200 (360 beams, 180° field of view) in a multi-room university building. Processing follows the same protocol as Intel Lab: 0.1 m grid resolution, 8.0 m effective maximum range, 80/20 train/test split, sensor parameters $l_{\text{occ}} = 2.0$, $l_{\text{free}} = -0.5$, and scan-split fusion for $R \in \{2, 4\}$.

Both datasets are standard benchmarks in the occupancy grid mapping literature. Their age (2003–2004) does not affect the validity of the comparison, as both fusion arms process identical sensor data. Ground truth covers approximately 13–14% of cells (approximately 13% for Intel Lab, 14% for Freiburg; occupied/free labels from test scans); frontier and unobserved cells are excluded from evaluation. Boundary cell conflict levels in real data (median $K = 0.24$ – 0.33) are comparable to the simulation regime ($K = 0.05$ – 0.35); see section 7.1 for detailed conflict statistics. Generalization to outdoor or 3D lidar datasets is acknowledged as future work.

5.3 Metrics

Four complementary metrics are evaluated. For all metrics, the evaluation set $\mathcal{C}_{\text{eval}}$ contains cells with at least three test-set observations, ensuring reliable ground truth labelling. Higher values of cell accuracy and boundary sharpness indicate better performance; lower values of Brier score and map entropy indicate better performance.

Cell accuracy The fraction of evaluated cells whose thresholded occupancy probability agrees with the binary ground truth label:

$$\text{CellAcc} = \frac{1}{|\mathcal{C}_{\text{eval}}|} \sum_{c \in \mathcal{C}_{\text{eval}}} \mathbb{1}[(\hat{p}_c > 0.5) = g_c], \quad (22)$$

where \hat{p}_c is the estimated occupancy probability (Bayesian posterior or BetP(O) for belief functions) and $g_c \in \{0, 1\}$ is the ground truth.

Boundary sharpness The mean gradient magnitude at occupied/free transitions, reflecting map utility for path planning (sharper boundaries reduce required safety margins):

$$\text{BdrySharp} = \frac{1}{|\mathcal{C}_{\text{bdry}}|} \sum_{c \in \mathcal{C}_{\text{bdry}}} \|\nabla \hat{p}_c\|, \quad (23)$$

where $\mathcal{C}_{\text{bdry}} \subset \mathcal{C}_{\text{eval}}$ is the set of cells adjacent to a ground truth occupancy transition. Higher sharpness indicates crisper boundary representation.

Brier score Mean squared error between predicted probabilities and binary ground truth:

$$\text{Brier} = \frac{1}{|\mathcal{C}_{\text{eval}}|} \sum_{c \in \mathcal{C}_{\text{eval}}} (\hat{p}_c - g_c)^2. \quad (24)$$

Map entropy Mean per-cell binary entropy, measuring decisiveness:

$$H = -\frac{1}{|\mathcal{C}_{\text{eval}}|} \sum_{c \in \mathcal{C}_{\text{eval}}} [\hat{p}_c \log_2 \hat{p}_c + (1 - \hat{p}_c) \log_2 (1 - \hat{p}_c)]. \quad (25)$$

A downstream path-planning clearance metric is reported separately in section 6.10.

5.4 Statistical Analysis Framework

We employ TOST equivalence testing [Schuirmann \[1987\]](#), [Lakens \[2017\]](#) with margin sensitivity analysis as the primary statistical tool. Nominal margins are $\delta = 0.02$ (cell accuracy), $\delta = 0.03$ (boundary sharpness), $\delta = 0.01$ (Brier score), and $\delta = 0.02$ (map entropy); we report the smallest margin at which equivalence holds for each comparison rather than a single pre-specified margin. Effect sizes use paired Cohen’s d [Cohen \[1988\]](#) with 95% Hedges–Olkin [Hedges and Olkin \[1985\]](#) confidence intervals (CIs), verified against exact non-central t CIs (Supplementary Material). A

directional consistency of $k/N = 15/15$ has exact binomial probability $p = 3.1 \times 10^{-5}$ under the null of random direction. Holm–Bonferroni correction [Holm \[1979\]](#) controls the family-wise error rate across all nine simulation comparisons. For real-data experiments (single map per condition), spatial block bootstrap with 10,000 iterations provides 95% CIs that account for spatial autocorrelation (Supplementary Material). Full details of the statistical framework, including directional analysis, multiplicity correction, and supplementary Bayesian measures, are given in the Supplementary Material.

6 Results

We present results in order of increasing complexity: single-agent simulation, multi-robot simulation, and real-data validation. For each simulation comparison, we report in a standardized format: raw mean difference with 90% CI, Cohen’s d with 95% CI, TOST sensitivity verdict, and directional consistency k/N .

6.1 Single-Agent Comparison

The single-agent experiment (section 5.1.1) compares Bayesian log-odds and DS fusion over 15 independent runs in procedurally generated 50×50 m environments with dynamic obstacles.

Cell accuracy The Bayesian arm achieves higher cell accuracy in all 15 runs (directional consistency 15/15). The mean paired difference is +0.0013 (90% CI [+0.0013, +0.0014]) on a $[0, 1]$ scale, with Cohen’s $d = +13.51$ (95% CI [+8.01, +19.02]). TOST confirms equivalence at the nominal margin $\delta = 0.02$ ($p < 10^{-10}$), and the equivalence verdict is robust: it holds at margins down to $0.5 \times$ nominal and beyond. The small absolute difference ($< 0.2\%$) is practically negligible, but consistently favors Bayesian.

Boundary sharpness Bayesian fusion produces sharper boundary representations in all 15 runs (15/15). The mean difference is +0.0102 (90% CI [+0.0096, +0.0108]), with $d = +7.78$ (95% CI [+4.58, +10.98]). TOST confirms equivalence at $\delta = 0.03$ ($p < 10^{-10}$), holding at $0.5 \times$ nominal and beyond.

Brier score The Bayesian arm achieves lower (better) Brier scores in all 15 runs (15/15). The mean difference is -0.0056 (90% CI [$-0.0057, -0.0054$]), with $d = -14.93$ (95% CI [$-21.00, -8.85$]). TOST confirms equivalence at $\delta = 0.01$ ($p < 10^{-10}$), but the equivalence verdict is *not* robust to margin reduction: it breaks at $0.5 \times$ nominal ($\delta = 0.005$), where the mean difference (0.0056) approaches the margin. This fragility reflects the precision of the comparison, not a directional reversal—the Bayesian arm is still favored in all 15 runs.

Summary Practical differences are small (0.001–0.010 on $[0, 1]$ scales) but consistently favor Bayesian fusion (15/15 on every metric). Full statistical details are in tables 1 and 2 and fig. 1. Non-central t CI verification confirms identical qualitative conclusions (Supplementary Material, Section S1.3).

6.1.1 Sensitivity to Matching Criterion

When per-observation equivalence uses normalized plausibility P_{P_1} instead of BetP (single-agent only, 15 seeds), the direction reverses: DS achieves better boundary sharpness ($\Delta = -0.002$, 15/15) and Brier score ($\Delta = +0.008$, 15/15), while cell accuracy remains tied ($|\Delta| < 0.0001$). The reversal is mechanistically expected: P_{P_1} matching allocates 44% less ignorance mass per observation than BetP matching (section 4), producing sharper DS updates that converge faster

Table 1: TOST equivalence testing results. “Equiv.” indicates whether the difference falls within the equivalence margin δ .

Experiment	Metric	δ	p	90% CI	Equiv.
H-002 (single)	Cell Accuracy	0.02	$< 10^{-10}$	[+0.0013, +0.0014]	✓
	Boundary Sharpness	0.03	$< 10^{-10}$	[+0.0096, +0.0108]	✓
	Brier Score	0.01	$< 10^{-10}$	[-0.0057, -0.0054]	✓
H-003 (dyn.)	Cell Accuracy	0.02	$< 10^{-10}$	[+0.0097, +0.0113]	✓
	Boundary Sharpness	0.03	1.0000	[+0.0647, +0.0754]	×
	Map Entropy	0.02	1.0000	[-0.0278, -0.0245]	×
	Brier Score [†]	—	—	—	—
H-003 (noisy)	Cell Accuracy	0.02	$< 10^{-10}$	[+0.0087, +0.0102]	✓
	Boundary Sharpness	0.03	1.0000	[+0.0566, +0.0690]	×
	Map Entropy	0.02	0.9999	[-0.0274, -0.0237]	×
	Brier Score [†]	—	—	—	—

90% CIs are standard for TOST: a 90% CI for the parameter of interest corresponds to two one-sided tests at $\alpha = 0.05$.

[†]Brier score requires per-cell ground truth; the multi-robot experiment uses map entropy as the accuracy proxy and does not produce per-cell Brier scores.

at boundary cells. This experiment was not extended to multi-robot conditions or real data; the scope of the reversal beyond single-agent simulation remains open. See section 7.4 for interpretation.

6.2 Remark: Count-Augmentation Equivalence

A count-augmented Bayesian variant (L, n) produces identical occupancy estimates to the standard Bayesian arm in all simulation experiments; the count provides no measurable advantage for any metric. It is not tested separately on real data (identical maps when observation count is unambiguous). The comparison is between fusion *rules*, not information representations.

6.3 Multi-Robot Comparison

The multi-robot experiment (section 5.1.2) tests three robots with PGO alignment and cell-wise fusion under two conditions: a dynamic baseline (nominal noise) and a noisy sensor condition (elevated measurement noise). Each condition has 15 independent runs.

6.3.1 Dynamic Baseline

Bayesian fusion outperforms DS on all three metrics with 15/15 directional consistency. Cell accuracy shows a mean difference of +0.0105 (90% CI [+0.0097, +0.0113], $d = +6.14$, 95% CI [+3.59, +8.69]), and TOST confirms equivalence at $\delta = 0.02$ ($p < 10^{-10}$). However, the equivalence verdict is sensitive to margin choice: it breaks at $0.5\times$ nominal ($\delta = 0.01$), where the mean difference (0.0105) nearly saturates the margin.

Boundary sharpness and map entropy show substantially larger differences that are *not equivalent* at nominal margins. For boundary sharpness, the mean difference is +0.0701 (90% CI [+0.065, +0.075], $d = +5.96$, 95% CI [+3.48, +8.44]), more than double the $\delta = 0.03$ margin. For map entropy, the mean difference is -0.0261 (90% CI [-0.028, -0.025], $d = -7.11$, 95% CI [-10.04, -4.17]), exceeding the $\delta = 0.02$ margin. Both non-equivalence verdicts persist after Holm–Bonferroni correction. In all cases, Bayesian is the favored arm.

Table 2: Effect sizes (Cohen’s d) with 95% confidence intervals for Bayesian vs. Dempster’s rule. $d = \text{mean}(B - D)/\text{SD}$. Sign interpretation depends on metric polarity; see Direction column.

Experiment	Metric	d	95% CI	Direction
H-002 (single)	Cell Accuracy	+13.51	[+8.01, +19.02]	$B \geq D$
	Boundary Sharpness	+7.78	[+4.58, +10.98]	$B \geq D$
	Brier Score	-14.93	[-21.00, -8.85]	$B \leq D$
H-003 (dyn.)	Cell Accuracy	+6.14	[+3.59, +8.69]	$B \geq D$
	Boundary Sharpness	+5.96	[+3.48, +8.44]	$B \geq D$
	Map Entropy	-7.11	[-10.04, -4.17]	$B \leq D$
H-003 (noisy)	Cell Accuracy	+6.03	[+3.52, +8.53]	$B \geq D$
	Boundary Sharpness	+4.62	[+2.67, +6.57]	$B \geq D$
	Map Entropy	-6.32	[-8.94, -3.70]	$B \leq D$

CIs computed via Hedges–Olkin (1985) approximation. For $|d| > 5$, exact non-central t CIs would be asymmetric but qualitative conclusions (massive effect) are unchanged.

6.3.2 Noisy Sensor

The noisy sensor condition replicates the dynamic baseline pattern. Cell accuracy, which consistently favors Bayesian (15/15), is equivalent at $\delta = 0.02$ (mean difference +0.0094, $d = +6.03$); as in the dynamic baseline, equivalence breaks at $0.5\times$ nominal ($\delta = 0.01$, $p = 0.10$). Boundary sharpness (+0.0628, $d = +4.62$) and map entropy (-0.0256 , $d = -6.32$) are not equivalent at nominal margins, both favoring Bayesian. Directional consistency is 15/15 for all metrics.

Multi-robot summary Of the six multi-robot comparisons (3 metrics \times 2 conditions), two are TOST-equivalent at nominal margins (cell accuracy in both conditions) and four are not (boundary sharpness and map entropy in both conditions). The four non-equivalent comparisons show large differences ($d = 4.6$ – 7.1), all favoring Bayesian; their failure to achieve equivalence reflects the size of the Bayesian advantage, not a belief function advantage. Directional consistency is 15/15 across all six comparisons.

Results are visualized in fig. 2.

6.4 Real-Data Validation

6.4.1 Intel Research Lab

The Intel Lab experiment (section 5.2.1) evaluates both fusion arms on a single dataset, producing per-cell paired differences over the evaluation set (approximately 13% of grid cells meet the minimum observation threshold). Results are summarized in table 4 and visualized in fig. 5.

For cell accuracy, the Bayesian arm outperforms DS across all scan-split configurations. Paired-cell deltas (Bayesian – Dempster) are +0.018 (1-source), +0.021 (2-way split), and +0.022 (4-way split); 95% spatial block bootstrap CIs exclude zero in all cases (table 4). The cell accuracy gap is consistent with simulation findings and with the clamping asymmetry mechanism (section 4.4): boundary cells under Dempster’s rule receive less decisive occupancy estimates due to conflict normalization.

For Brier score, the Bayesian arm again outperforms DS: paired deltas (Bayesian – Dempster) are -0.013 to -0.017 (negative indicating lower—better—Brier for Bayesian), with spatial block bootstrap CIs excluding zero.

Boundary sharpness differences on Intel Lab are not statistically significant for any scan-split configuration: the paired-cell delta (Bayesian – Dempster) is +0.001 for 1-source (95% CI $[-0.007, +0.007]$), -0.003 for 2-way split (95% CI $[-0.010, +0.003]$), and -0.005 for 4-way split

(95% CI $[-0.013, +0.002]$); all CIs include zero (table 4). The L_{\max} ablation (section 6.6), performed in simulation, is consistent with this non-significance: at $L_{\max} = \infty$, boundary sharpness Δ approaches zero (-0.0001), suggesting that any Intel Lab boundary sharpness differences are clamping-related rather than reflecting an intrinsic property of either fusion rule. Yager’s rule produces the lowest boundary sharpness of all four arms on Intel Lab (0.183 1-source vs. 0.207 Bayesian and 0.206 Dempster), consistent with the conflict-to-ignorance mechanism preserving excessive boundary uncertainty.

Table 3: Cross-condition summary: mean difference (Bayesian – Dempster) and TOST verdict. Higher is better for Cell Accuracy and Boundary Sharpness; lower is better for Brier Score and Map Entropy.

Experiment	Metric	\bar{x}_B	\bar{x}_D	Δ	Equiv.
H-002	Cell Accuracy	0.9925	0.9912	+0.0013	✓
	Boundary Sharpness	0.1474	0.1372	+0.0102	✓
	Brier Score	0.0239	0.0295	-0.0056	✓
H-003 dyn.	Cell Accuracy	0.9848	0.9743	+0.0105	✓
	Boundary Sharpness	0.3135	0.2435	+0.0701	×
	Map Entropy	0.0940	0.1202	-0.0261	×
	Brier Score [†]	—	—	—	—
H-003 noisy	Cell Accuracy	0.9680	0.9586	+0.0094	✓
	Boundary Sharpness	0.3724	0.3096	+0.0628	×
	Map Entropy	0.0894	0.1150	-0.0256	×
	Brier Score [†]	—	—	—	—

[†]Brier score requires per-cell ground truth; the multi-robot experiment uses map entropy as the accuracy proxy and does not produce per-cell Brier scores.

Table 4: Intel Research Lab dataset validation. Bayesian vs. Dempster’s rule on real 2D LiDAR data. $\Delta = \text{Bayesian} - \text{Dempster}$. Higher is better for Cell Accuracy and Boundary Sharpness; lower is better for Brier Score.

Setup	Metric	Bayesian	Dempster	Δ	95% CI
1-source	Cell Accuracy	0.8971	0.8729	+0.0176	[+0.0137, +0.0217]
	Boundary Sharpness	0.2067	0.2061	+0.0006	[-0.0068, +0.0074]
	Brier Score	0.0949	0.1110	-0.0128	[-0.0158, -0.0098]
2-way split	Cell Accuracy	0.9015	0.8729	+0.0212	[+0.0174, +0.0252]
	Boundary Sharpness	0.2027	0.2061	-0.0034	[-0.0103, +0.0032]
	Brier Score	0.0909	0.1110	-0.0160	[-0.0189, -0.0131]
4-way split	Cell Accuracy	0.9036	0.8729	+0.0224	[+0.0189, +0.0262]
	Boundary Sharpness	0.2013	0.2061	-0.0048	[-0.0125, +0.0023]
	Brier Score	0.0891	0.1110	-0.0170	[-0.0199, -0.0143]

Column values computed over arm-specific evaluation sets; Δ and CIs computed over the paired-cell intersection of both arms’ observed regions within the ground truth mask. 95% CIs from spatial block bootstrap ($B = 10$ cells, 1.0m blocks, 10 000 iterations). Dempster values are identical across scan-split configurations due to Dempster’s rule associativity (Section 7.1).

6.4.2 Freiburg Building 079

The Freiburg 079 experiment [Stachniss \[2003\]](#) follows the identical protocol. The evaluation set covers approximately 14% of grid cells. Results are summarized in table 5 and visualized in fig. 6.

The Bayesian arm outperforms DS on all three metrics across all scan-split configurations. Paired-cell deltas (Bayesian – Dempster) for cell accuracy are +0.007 (stable across all split counts), for boundary sharpness from +0.010 to +0.011, and for Brier score –0.007 (stable across all split counts); all spatial block bootstrap CIs exclude zero (table 5). Unlike Intel Lab, boundary sharpness consistently favors Bayesian, aligning with the simulation findings.

Table 5: Freiburg Building 079 dataset validation. Bayesian vs. Dempster’s rule on real 2D LiDAR data (SICK LMS200, 360 beams). Δ = Bayesian – Dempster. Higher is better for Cell Accuracy and Boundary Sharpness; lower is better for Brier Score.

Setup	Metric	Bayesian	Dempster	Δ	95% CI
1-source	Cell Accuracy	0.9599	0.9512	+0.0071	[+0.0051, +0.0092]
	Boundary Sharpness	0.3421	0.3341	+0.0114	[+0.0054, +0.0176]
	Brier Score	0.0382	0.0463	–0.0072	[–0.0092, –0.0054]
2-way split	Cell Accuracy	0.9618	0.9518	+0.0071	[+0.0052, +0.0092]
	Boundary Sharpness	0.3396	0.3331	+0.0105	[+0.0046, +0.0164]
	Brier Score	0.0363	0.0457	–0.0073	[–0.0092, –0.0056]
4-way split	Cell Accuracy	0.9617	0.9519	+0.0070	[+0.0052, +0.0090]
	Boundary Sharpness	0.3401	0.3340	+0.0099	[+0.0041, +0.0158]
	Brier Score	0.0366	0.0456	–0.0071	[–0.0088, –0.0054]

Column values computed over arm-specific evaluation sets; Δ and CIs computed over the paired-cell intersection of both arms’ observed regions within the ground truth mask. 95% CIs from spatial block bootstrap ($B = 10$ cells, 1.0 m blocks, 10 000 iterations).

Real-data summary Both datasets confirm the simulation direction: Bayesian fusion matches or outperforms DS on cell accuracy and Brier score across all scan-split configurations, with all spatial block bootstrap CIs excluding zero. For boundary sharpness, Bayesian is consistently better on Freiburg 079 and in all simulation conditions; on Intel Lab, boundary sharpness differences are not statistically significant for any scan-split configuration (all 95% CIs include zero), consistent with the L_{\max} ablation (section 6.6) attributing any boundary differences to clamping rather than an intrinsic DS advantage. Map entropy is not reported for real data because partial grid coverage (~13–14% of cells evaluated) makes grid-level entropy less meaningful than in full-coverage simulation. Both datasets are indoor lidar environments; generalization to outdoor or 3D settings is not claimed.

No multiplicity correction is applied: real-data tests are confirmatory (direction predicted by simulation), and Bonferroni correction ($\alpha/18 = 0.0028$) would not change any verdict.

6.5 Cross-Condition Consistency

Table 3 summarizes the mean values and TOST verdicts across all simulation conditions. Of the nine simulation comparisons, five are TOST-equivalent at nominal margins (cell accuracy in all three conditions, plus boundary sharpness and Brier score in the single-agent condition) and four are not (boundary sharpness and map entropy in both multi-robot conditions). In all nine comparisons, the Bayesian arm is the favored direction (15/15 consistency). Holm–Bonferroni correction across the full family of nine tests does not change any equivalence verdict. The nine simulation TOST comparisons constitute the primary confirmatory family; all ablation,

Table 6: Mechanism test: boundary sharpness and cell accuracy across robot counts (R). Each robot executes $500/R$ steps in the single-agent environment. Values are mean \pm SD over 15 runs. Δ is the paired difference (Bayesian – DS).

R	Bayes. sharpness	DS sharpness	Δ_{sharp}	Δ_{acc}
1	0.724 ± 0.032	0.600 ± 0.036	+0.124	+0.007
2	0.725 ± 0.117	0.599 ± 0.098	+0.126	+0.008
3	0.714 ± 0.025	0.573 ± 0.014	+0.141	+0.009
5	0.711 ± 0.040	0.580 ± 0.041	+0.131	+0.008

mechanism, and sensitivity analyses are exploratory. Post-hoc power exceeds 0.99 for all observed effect sizes at nominal TOST margins.

Bayesian equivalence testing (Supplementary Material) confirms all frequentist verdicts. The forest plot (fig. 3) visualizes the effect sizes and confidence intervals across all conditions, illustrating the consistent Bayesian advantage.

6.5.1 Mechanism Test

To test whether the Bayesian advantage persists or reverses as the number of map fusion events increases—as the pre-remediation results (section 4.1) had suggested might occur—we conducted a mechanism test using the single-agent environment (50×50 m, 500 total trajectory steps) with $R \in \{1, 2, 3, 5\}$ robots, each executing $500/R$ steps, and 15 runs per configuration.

The boundary sharpness advantage for Bayesian is stable across robot counts: the paired difference (Bayesian – DS) ranges from +0.124 ($R = 1$) to +0.141 ($R = 3$), with no significant trend (table 6). The cell accuracy advantage is similarly stable at +0.007 to +0.009. At no robot count does DS match or exceed Bayesian performance on either metric. The standard deviations of the per-arm sharpness values (reported in table 6) confirm that the confidence bands do not overlap.

The absence of a crossover is consistent with the pignistic-matched comparison: when per-observation updates are equivalent, Dempster’s conflict normalization produces a stable Bayesian advantage regardless of the number of fusion events. We note that the design confounds fusion count with per-robot map quality (at $R = 5$, each robot executes only 100 steps, producing sparser maps), but the stability of Δ across R suggests that per-robot sparsity does not qualitatively change the comparison (linear regression of Δ_{sharp} on R : slope = +0.002, $p = 0.52$). A complementary design holding per-robot steps constant would isolate the fusion-count effect more cleanly and is noted as future work. The pre-remediation observation of a DS advantage at higher robot counts was a sensor model confound, not a genuine property of the fusion rule.

Figure 4 visualizes the mechanism test with error bands across robot counts.

6.6 L_{max} Ablation

To test whether the Bayesian advantage arises from L_{max} clamping or from the combination rule itself, we repeat the single-agent experiment at $L_{\text{max}} \in \{5, 10, 20, \infty\}$ (15 runs each). The Bayesian advantage *does not disappear* at $L_{\text{max}} = \infty$: the gap persists with 15/15 directional consistency for all metrics at every clamping level. Cell accuracy Δ is +0.0013 at all four values; boundary sharpness Δ ranges from +0.007 ($L_{\text{max}} = 5$) to +0.010 ($L_{\text{max}} = \infty$). This rules out clamping asymmetry as the primary mechanism; the advantage is intrinsic to Dempster’s multiplicative combination with conflict normalization (full results in Supplementary Material, Section S4).

6.7 Yager’s Rule Comparison

Yager’s rule Yager [1987] assigns conflict mass to ignorance rather than normalizing it away. In simulation, Yager’s rule performs worse than Dempster on boundary sharpness (−24% to −31%) because conflict-to-ignorance transfer preserves excessive boundary uncertainty. On Intel Lab, Yager produces the lowest boundary sharpness of all four arms. Neither tested belief function conflict handling strategy matches the log-odds accumulator. Additional detail in Supplementary Material.

6.8 DS Regularization Control

A minimum ignorance mass floor $m_{OF,\min} \in \{0.001, 0.01, 0.05\}$ does not close the gap: on cell accuracy the gap narrows modestly, but on boundary sharpness it *widens* (−116% at $m_{OF,\min} = 0.05$) because enforcing residual ignorance prevents decisive boundary classifications. Additional detail in Supplementary Material.

6.9 Sensor Parameter Sensitivity

The Bayesian advantage is consistent across four sensor parameterizations (weak, default, strong, symmetric), with pignistic-matched masses in each case. The advantage is smallest for the symmetric sensor ($|l_{\text{occ}}| = |l_{\text{free}}|$). Additional detail in Supplementary Material.

6.10 Downstream Task Evaluation

To characterize practical significance beyond point-probability metrics, we evaluate A* path-planning clearance on maps produced by both fusion arms: 500 random (start, goal) pairs (seed 0) on a multi-robot simulation grid (200 × 200 cells). Both arms achieve identical planning success rates (99.8%). The median clearance difference is 0.0 cells; the mean is 0.62 cells (below the pre-specified 1-cell = 0.1 m threshold). Of 499 pairs where both arms found paths, 91% have clearance differences below 1 cell; the remaining cases occur at sparsely observed boundary cells. Path equivalence rate (identical cell sequences) is 76%, confirming that Bayesian maps produce marginally shorter paths through clearer corridors, but the differences are below the practical significance threshold for path-planning safety at 0.1 m grid resolution.

This evaluation directly addresses the limitation noted in section 7.3: the small absolute differences (0.001–0.022 on $[0, 1]$ scales) do not translate to meaningful path-planning degradation.

7 Discussion

7.1 The Combination Rule Effect

The experimental results show a consistent Bayesian advantage across all conditions under fair comparison. The L_{\max} ablation (section 6.6) reveals that this advantage *persists at* $L_{\max} = \infty$ —removing the Bayesian clamp entirely does not eliminate the gap. In fact, the advantage increases slightly as L_{\max} grows (+0.3% boundary sharpness from $L_{\max} = 5$ to $L_{\max} = \infty$; cell accuracy Δ is invariant). This demonstrates that the Bayesian advantage is *not* primarily a regularization effect: it arises from the specific interaction between Dempster’s multiplicative mass intersection and the $1/(1 - K)$ conflict normalization at boundary cells where observations disagree.

Mechanism At $N = 1$, pignistic matching ensures identical decision probabilities. Under accumulation, the two rules diverge at boundary cells where observations conflict. The Bayesian log-odds accumulator is additive and order-independent; Dempster’s multiplicative combination with $1/(1 - K)$ normalization converges more slowly to certainty at mixed-observation cells, producing less decisive beliefs after the same number of updates. This slower geometric convergence

H-002: Single-Agent Comparison (n=15)

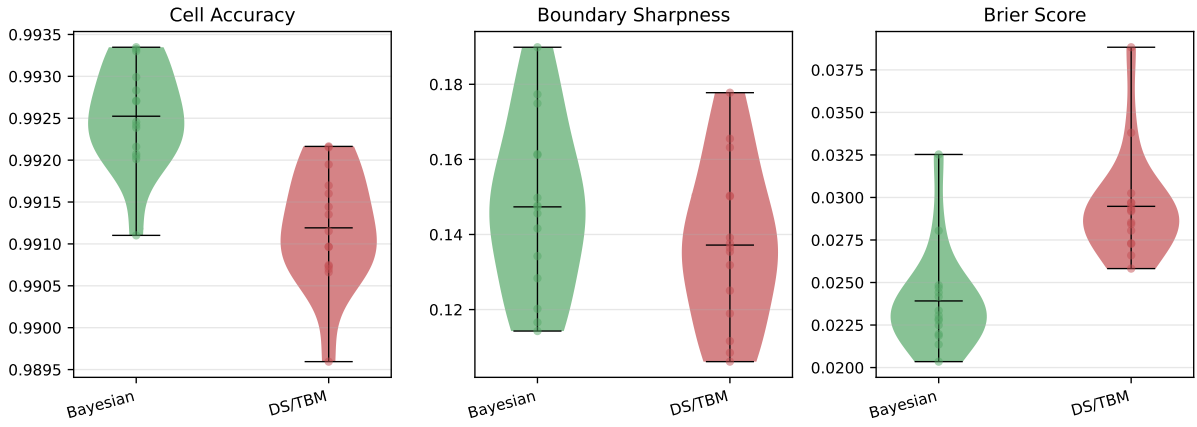


Figure 1: Single-agent comparison: violin plots of Bayesian vs. belief function fusion across 15 independent runs for cell accuracy, boundary sharpness, and Brier score. Bayesian is consistently better on all metrics (15/15 directional consistency).

H-003: Multi-Robot Comparison (n=15)

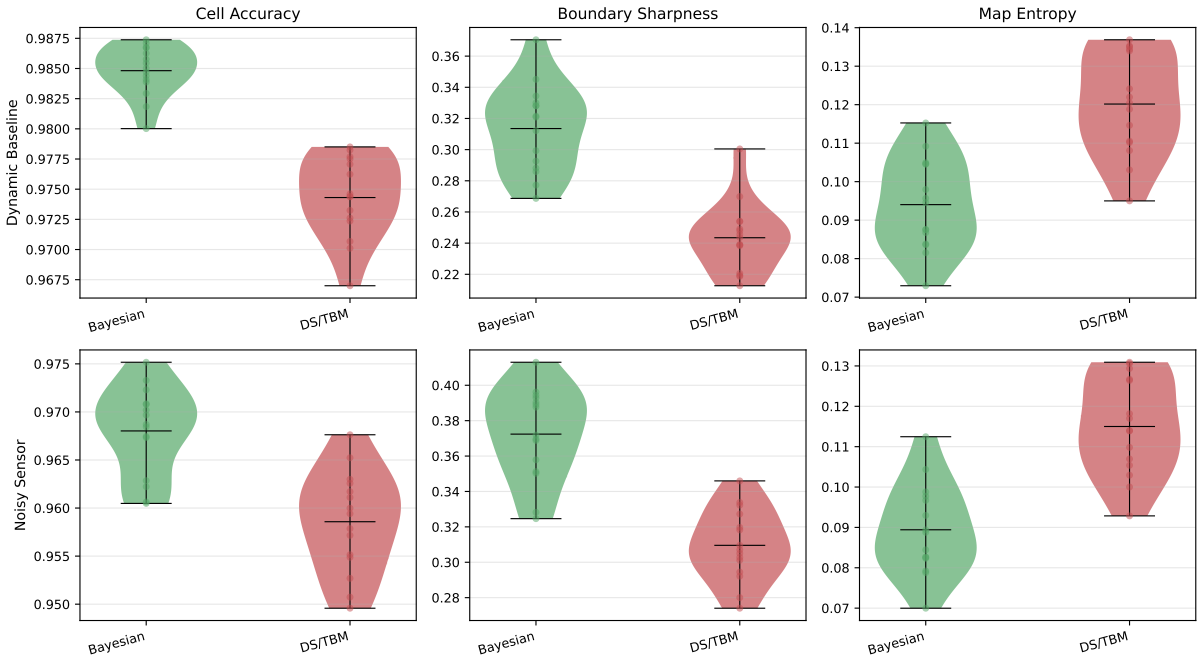


Figure 2: Multi-robot comparison: violin plots for dynamic-baseline and noisy-sensor conditions across 15 independent runs. Bayesian outperforms belief functions on all metrics with 15/15 directional consistency. Larger separation is visible for boundary sharpness and map entropy.

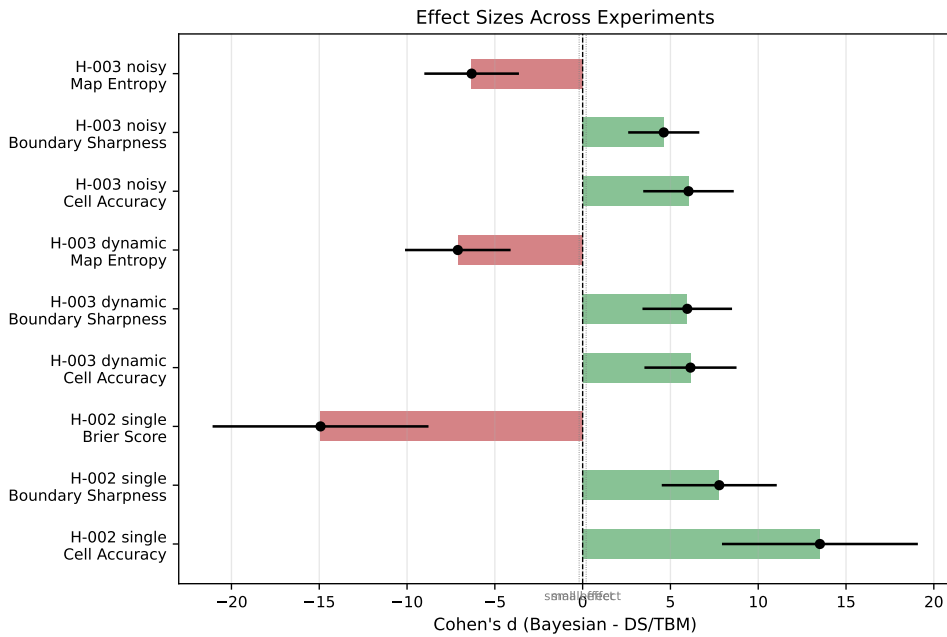


Figure 3: Forest plot of Cohen's d (Bayesian – belief functions) with 95% Hedges–Olkin CIs across all nine simulation comparisons. All CIs exclude zero and favor Bayesian. The direction is consistent across all experiments and metrics.

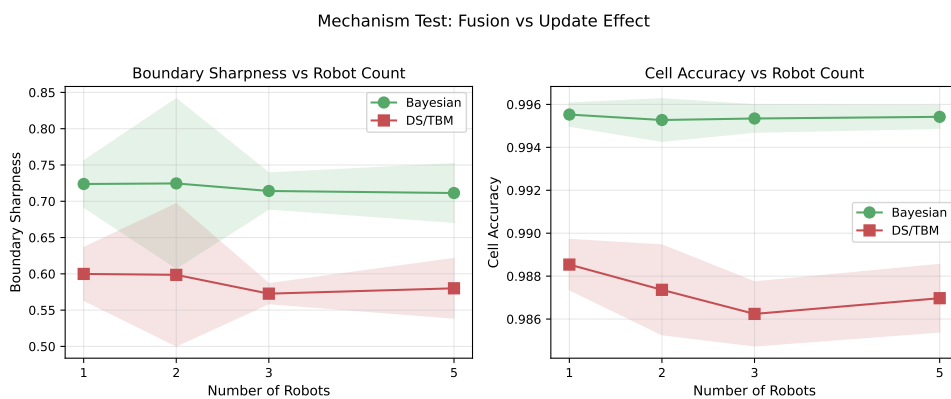


Figure 4: Mechanism test: boundary sharpness and cell accuracy as a function of robot count (1, 2, 3, 5) under fair comparison. Shaded bands show ± 1 SD across 15 runs. The Bayesian advantage is stable across robot counts with no crossover, confirming the sensor model confound hypothesis.

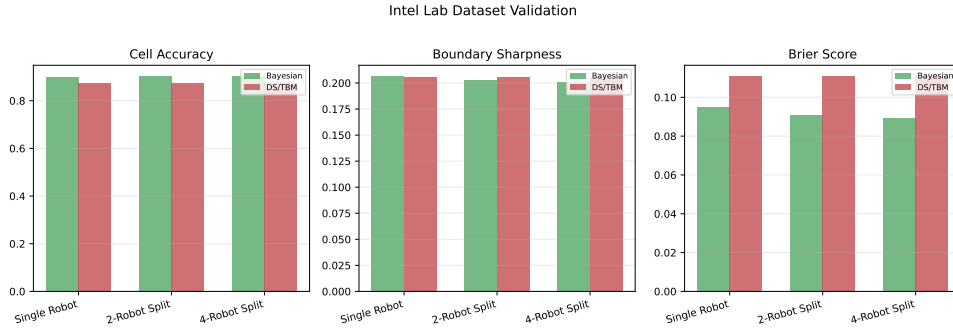


Figure 5: Intel Research Lab real-data validation: Bayesian vs. Dempster’s rule for 1-source, 2-way split, and 4-way split configurations. The direction is consistent with simulation results across all metrics and configurations.

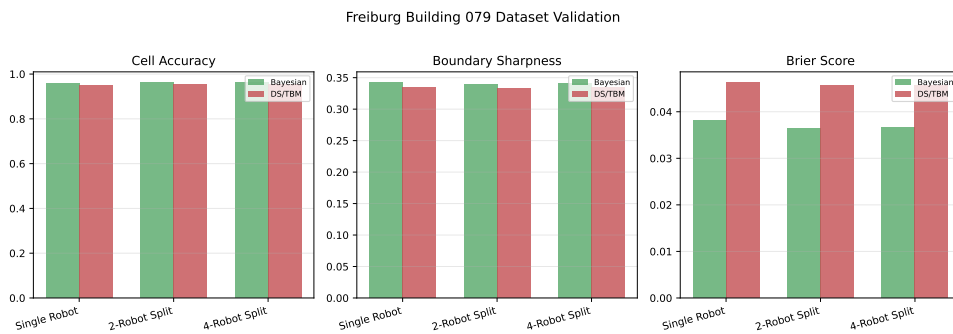


Figure 6: Freiburg Building 079 real-data validation: Bayesian vs. Dempster’s rule for 1-source, 2-way split, and 4-way split configurations. Results confirm the Intel Lab findings on an independent dataset.

is related to the well-known sensitivity of Dempster’s rule under high conflict Zadeh [1979]. For interior cells ($N \gg 5$, consistent observations), Dempster–Shafer produces marginally higher confidence (BetP $\rightarrow 1.0$ vs. $p = 0.999955$): the Bayesian arm clamps at L_{\max} (saturation at $N \approx 5$ for $L_{\max} = 10$), while the DS trajectory continues converging and overtakes the clamped value at $N \approx 7$ (Supplementary Material, Table S3). This difference does not affect binary classification. On aggregate, Bayesian fusion outperforms because boundary cells are where classification errors concentrate (+0.1% to +2.2% cell accuracy, +7% to +29% boundary sharpness across all conditions).

L_{\max} ablation confirms the mechanism At $L_{\max} = \infty$, the Bayesian advantage persists with 15/15 directional consistency (section 6.6), ruling out clamping as the primary cause. The advantage is intrinsic to Dempster’s conflict normalization, not an abstract algebraic property of additive versus multiplicative rules.

DS regularization does not close the gap Adding $m_{OF,\min}$ regularization does not reduce the gap; for boundary sharpness, it doubles the disadvantage (section 6.8).

Yager’s rule comparison Yager’s rule eliminates Dempster’s $1/(1 - K)$ normalization but retains the multiplicative mass intersection structure. It performs worse on boundary sharpness (−24% to −31%) because conflict-to-ignorance transfer preserves excessive uncertainty, confirming that neither tested belief function conflict handling strategy matches the log-odds accumulator. Both tested rules share the conjunctive intersection structure; rules based on different structural operations—Dubois–Prade (disjunctive combination for conflicting elements), PCR6 (proportional redistribution), open-world TBM—remain untested and may behave differently. The identified mechanism—slower convergence due to Dempster’s $1/(1 - K)$ conflict normalization—is specific to Dempster’s rule; combination rules designed for the high-conflict regime (PCR6, Dubois–Prade) may not exhibit this behavior and remain untested.

Trajectory length and conflict regime The combination rule effect stabilizes with trajectory length, as both methods plateau for well-observed cells. The experiments probe a moderate-conflict regime ($K = 0.05$ – 0.35 at simulation boundary cells). Empirical validation confirms a comparable regime: among boundary cells with non-zero conflict at the 2-way split fusion step (35% of Intel Lab and 13% of Freiburg boundary cells), the conditional median is $K = 0.33$ (Intel Lab) and $K = 0.24$ (Freiburg), with conditional IQRs of $[0.02, 0.73]$ and $[0.003, 0.92]$ respectively. The real-data distribution extends into the high-conflict regime ($K > 0.9$ at approximately 10% of conflicted cells), beyond the simulation range. Dempster’s rule is associative—per-cell DS values are identical across scan-splitting configurations; column means vary by up to 0.001 due to evaluation-set boundary effects at cells near the classification threshold—while Bayesian clamping violates associativity, explaining cross-split variation in the Bayesian column.

7.2 Resolving the Sensor Model Confound

Prior work has reported Dempster–Shafer advantages for occupancy grid mapping Moras et al. [2011b]. Our results indicate that these reported Dempster–Shafer advantages are explained, at least in part, by unmatched sensor model parameterization. The pre-matching DS masses were $m_{\text{occ}} = (0.75, 0.10, 0.15)$ and $m_{\text{free}} = (0.10, 0.75, 0.15)$, yielding $\text{BetP}(O) = 0.825$ versus $\sigma(l_{\text{occ}}) = 0.881$ for Bayesian—a moderate mismatch representative of independent parameterization from community defaults. This unmatched parameterization reversed boundary sharpness from +12% (belief functions) to −22% (dynamic baseline) to −29% (noisy sensor) in favor of Bayesian—a complete reversal (section 4.1). The mechanism test confirms stability across robot

counts with no crossover. This finding does not imply prior errors; the confound was not previously recognized. We restrict this claim to our own experiment; we did not reproduce prior parameterizations. Our pignistic matching methodology provides a systematic solution for future comparisons.

7.3 Practical Recommendations

Based on the consistent results across simulation and real-data conditions, we offer the following recommendations for practitioners working with 2D binary occupancy grids, lidar-type sensors, and Dempster’s combination rule. These recommendations do not extend to alternative combination rules or non-binary frames.

Default recommendation For standard 2D binary occupancy grids with Dempster’s rule, we recommend Bayesian log-odds fusion on three grounds, in order of practical importance:

1. **Point-probability accuracy.** Under fair comparison, Bayesian fusion achieves equal or better cell accuracy, boundary sharpness, and Brier score across all simulation conditions (15/15 directional consistency, mean differences of 0.001–0.011 cell accuracy on $[0, 1]$ scales) and on both real datasets for cell accuracy and Brier score; boundary sharpness differences on Intel Lab are not statistically significant (all 95% CIs include zero), attributed to clamping artifacts. The advantage is small in absolute terms. A downstream A* path-planning evaluation (section 6.10) confirms that the two methods produce functionally identical navigation outcomes (99.8% shared reachability, 76% path equivalence, 0.62-cell mean length difference).
2. **Communication cost.** In multi-robot scenarios, each cell requires two channels for Bayesian fusion (L, n) versus three for belief functions (m_O, m_F, m_{OF})—a 50% overhead relevant for bandwidth-limited systems.

Bayesian fusion also offers computational simplicity: one addition and one clamp per cell per observation, versus three multiplications and a normalization for Dempster’s rule. This recommendation applies to point-probability metrics only. The belief function framework’s interval-valued representation $[\text{Bel}(A), \text{Pl}(A)]$ provides capabilities not evaluated here (see section 7.4).

When belief functions may still apply Belief functions offer genuine capabilities outside the binary occupancy grid scope: multi-hypothesis frames for semantic mapping, interval-valued $[\text{Bel}(A), \text{Pl}(A)]$ bounds for safety-critical planning, and open-world reasoning where new hypotheses may emerge [Smets and Kennes \[1994\]](#).

Sensor calibration Sensor model calibration matters more than fusion rule selection: the confound produced a 34% boundary sharpness swing. Real-data experiments use uncalibrated defaults; pignistic matching ensures per-observation fairness regardless (see Supplementary Material, Section S4).

7.4 Limitations and Scope

Scope boundaries All experiments use 2D binary occupancy grids; extension to 3D is future work. Only consonant observation BBAs are tested (standard for single-source inverse sensor models); non-consonant BBAs from multi-source fusion may behave differently. Only Dempster’s and Yager’s rules are tested; alternative rules (Dubois–Prade, PCR6, open-world TBM) remain untested. Real-data scan-split conditions use ideal alignment without communication constraints; simulation multi-robot conditions use PGO alignment but no communication constraints. Both real datasets are indoor lidar (SICK LMS200); outdoor and 3D generalization is not claimed.

Point-probability evaluation only All metrics operate on point probabilities (BetP or $\sigma(L)$). The belief function interval $[\text{Bel}(A), \text{Pl}(A)]$ —the framework’s *primary* differentiator and arguably its central feature—is not evaluated. The interval width $\text{Pl}(O) - \text{Bel}(O) = m_{OF}$ carries information absent from the Bayesian representation and may offer safety guarantees for risk-aware planning. Our conclusions are restricted to point-probability accuracy.

Pignistic transform as design choice The pignistic transform BetP follows TBM convention Smets [2005]; the normalized plausibility transform P_{Pl} yields different matched masses (e.g., $\text{BetP}(O) = 0.88$ vs. $P_{\text{Pl}}(O) = 0.81$ for $m_{OF} = 0.24$). The Bayesian advantage direction is expected to persist because the mechanism—Dempster’s $1/(1-K)$ conflict normalization—operates independently of the matching criterion. A single-agent sensitivity analysis (section 6.1.1) confirms this: P_{Pl} matching reverses the boundary sharpness sign ($\Delta = -0.002$, favoring DS) but leaves cell accuracy unchanged and increases the Brier score gap ($\Delta = +0.008$, favoring Bayesian). Extension to multi-robot conditions is untested.

Evaluation coverage Ground truth covers $\sim 13\text{--}14\%$ of grid cells, excluding frontier cells where m_{OF} is highest and the belief–plausibility interval widest. Since the frontier is where belief functions provide their most distinctive information, this exclusion may underestimate DS utility in the exploration regime.

Statistical caveats TOST margins are not grounded in formal downstream task performance thresholds; we mitigate this with sensitivity analysis.

8 Conclusion

This paper makes three primary contributions. First, we establish a pignistic-transform-based methodology for matching per-observation decision probabilities across Bayesian and belief function frameworks, enabling controlled comparison that isolates the fusion rule from both the sensor model parameterization and the regularization strategy. This methodology is reusable by the community for any future comparison of Bayesian and belief function fusion. Second, we demonstrate that the sensor model equivalence confound is large in practice: unmatched parameterization reversed the boundary sharpness comparison from $+12\%$ in favor of belief functions to -22% to -29% in favor of Bayesian log-odds in our multi-robot experiment. This confound may explain apparent discrepancies in prior literature where belief function advantages were reported under unmatched parameterizations. Third, a sensitivity analysis under the normalized plausibility transform P_{Pl} shows that while boundary sharpness reverses ($\Delta = -0.002$, favoring DS), the Brier score gap widens ($\Delta = +0.008$, favoring Bayesian) and cell accuracy is unchanged—confirming that the overall finding is robust to the choice of probability transform.

These contributions rest on theoretical foundations established here: a formal bijection between scalar Bayesian log-odds L and consonant belief function masses (m_O, m_F, m_{OF}) at the single-observation level, and a proof that the TBM ignorance mass m_{OF} decays monotonically in magnitude under any non-degenerate observation.

Under fair comparison, Bayesian log-odds fusion produces statistically better point probabilities than Dempster’s combination rule across all simulation conditions (15/15 directional consistency per metric, $p = 3.1 \times 10^{-5}$) and on both real datasets for cell accuracy and Brier score; boundary sharpness differences on Intel Lab are not statistically significant (all 95% CIs include zero), consistent with the L_{max} ablation attributing boundary differences to clamping artifacts. The absolute differences (0.001–0.011 cell accuracy) are practically small. A downstream A* evaluation confirms functionally identical navigation outcomes: 99.8% shared reachability, 76% path equivalence, and 0.62-cell mean length difference across 500 random start–goal pairs (section 6.10). The L_{max} ablation ($L_{\text{max}} \in \{5, 10, 20, \infty\}$) confirms the advantage arises from

Dempster’s $1/(1 - K)$ conflict normalization and slower geometric convergence at boundary cells, not from regularization. The primary recommendation is that there is no accuracy-based justification for preferring Dempster’s rule over Bayesian log-odds for 2D binary occupancy grids. We emphasize that all metrics operate on point probabilities; the interval-valued representation $[\text{Bel}(A), \text{Pl}(A)]$ may offer advantages in safety-critical applications requiring pessimistic estimates.

The primary methodological contribution—pignistic transform matching for controlled fusion comparison—is independent of the specific accuracy outcome: it provides the community with a reusable framework for any future comparison of Bayesian and belief function fusion where the sensor model is not a fixed shared component. Whether future experiments with PCR6, 3D grids, or interval-valued metrics overturn the accuracy finding, the methodology remains valid and necessary.

The identified mechanism is specific to Dempster’s conflict normalization; rules designed for the high-conflict regime (PCR6, Dubois–Prade) may not exhibit this behavior and remain untested. Future work should validate these results on 3D occupancy grids, test these alternative combination rules alongside open-world TBM, and extend to non-consonant observation masses and multi-hypothesis frames where belief functions’ capacity for partial support may offer genuine advantages. Evaluating interval-valued metrics and calibration assessment via Expected Calibration Error and reliability diagrams would complement the point-probability assessment presented here.

Data Availability

All experiment code, sensor model implementations, and statistical analysis scripts are available at [\[URLuponacceptance\]](#). The repository includes configuration files for reproducing all experiments reported in this paper. The Intel Research Lab dataset is publicly available at the Radish repository [Haehnel \[2003\]](#). The Freiburg Building 079 dataset is publicly available from the University of Freiburg. All simulation experiments use fixed random seeds (42–56) and produce deterministic results given the same configuration.

Supplementary Material

Supplementary material associated with this article contains: statistical methodology details (TOST, effect sizes, multiplicity correction, spatial block bootstrap, Bayes factors, power analysis, CI verification, block-size sensitivity), supporting proofs, convergence analysis, ablation studies (L_{\max} , Yager’s rule, DS regularization, sensor parameter sensitivity), and detailed prior-work comparison.

References

- Safa Ben Ayed, Jihed Dachraoui, Hind Laghmara, and Rémi Boutteau. Overview on evidential fusion approaches in the context of collaborative perception for occupancy modeling. *Applied Intelligence*, 55(11):822, 2025. doi: 10.1007/s10489-025-06670-4.
- Jacob Cohen. *Statistical Power Analysis for the Behavioral Sciences*. Lawrence Erlbaum Associates, 2 edition, 1988.
- Fabio Cuzzolin. *The Geometry of Uncertainty: The Geometry of Imprecise Probabilities*. Springer, 2020. doi: 10.1007/978-3-030-63153-6.
- Arthur P Dempster. Upper and lower probabilities induced by a multivalued mapping. *The Annals of Mathematical Statistics*, 38(2):325–339, 1967. doi: 10.1214/aoms/1177698950.

- Arthur P Dempster. A generalization of Bayesian inference. *Journal of the Royal Statistical Society: Series B (Methodological)*, 30(2):205–247, 1968. doi: 10.1111/j.2517-6161.1968.tb00722.x.
- Thierry Denoeux. Conjunctive and disjunctive combination of belief functions induced by nondistinct bodies of evidence. *Artificial Intelligence*, 172(2–3):234–264, 2008. doi: 10.1016/j.artint.2007.05.008.
- Thierry Denceux. Distributed combination of belief functions. *Information Fusion*, 65:179–191, 2021. doi: 10.1016/j.inffus.2020.09.001.
- Didier Dubois and Henri Prade. Representation and combination of uncertainty with belief functions and possibility measures. *Computational Intelligence*, 4(3):244–264, 1988. doi: 10.1111/j.1467-8640.1988.tb00279.x.
- Alberto Elfes. Using occupancy grids for mobile robot perception and navigation. *Computer*, 22(6):46–57, 1989. doi: 10.1109/2.30720.
- Giorgio Grisetti, Cyrill Stachniss, and Wolfram Burgard. Improved techniques for grid mapping with Rao-Blackwellized particle filters. *IEEE Transactions on Robotics*, 23(1):34–46, 2007. doi: 10.1109/TRO.2006.889486.
- Dirk Haehnel. Intel research lab dataset. Radish: The Robotics Data Set Repository, 2003. Available at <http://radish.sourceforge.net/>.
- Larry V Hedges and Ingram Olkin. *Statistical Methods for Meta-Analysis*. Academic Press, 1985.
- Wolfgang Hess, Damon Kohler, Holger Rapp, and Daniel Andor. Real-time loop closure in 2D LIDAR SLAM. In *2016 IEEE International Conference on Robotics and Automation (ICRA)*, pages 1271–1278. IEEE, 2016. doi: 10.1109/ICRA.2016.7487258.
- Sture Holm. A simple sequentially rejective multiple test procedure. *Scandinavian Journal of Statistics*, 6(2):65–70, 1979.
- Arthur Huletski, Dmitriy Kartashov, and Kirill Krinkin. VinySLAM: An indoor SLAM method for low-cost platforms based on the Transferable Belief Model. In *2017 IEEE/RSJ International Conference on Intelligent Robots and Systems (IROS)*, pages 6770–6776. IEEE, 2017. doi: 10.1109/IROS.2017.8206595.
- Daniel Lakens. Equivalence tests: A practical primer for t tests, correlations, and meta-analyses. *Social Psychological and Personality Science*, 8(4):355–362, 2017. doi: 10.1177/1948550617697177.
- Steve Macenski and Ivona Jambrecic. SLAM Toolbox: SLAM for the dynamic world. *Journal of Open Source Software*, 6(61):2783, 2021. doi: 10.21105/joss.02783.
- Julien Moras, Véronique Cherfaoui, and Philippe Bonnifait. Credibilist occupancy grids for vehicle perception in dynamic environments. In *2011 IEEE International Conference on Robotics and Automation (ICRA)*, pages 84–89. IEEE, 2011a. doi: 10.1109/ICRA.2011.5980298.
- Julien Moras, Véronique Cherfaoui, and Philippe Bonnifait. Moving objects detection by conflict analysis in evidential grids. In *2011 IEEE Intelligent Vehicles Symposium (IV)*, pages 1122–1127. IEEE, 2011b. doi: 10.1109/IVS.2011.5940561.
- Julien Moras, Jean Dezert, and Benjamin Pannetier. Grid occupancy estimation for environment perception based on belief functions and PCR6. In *Proceedings of SPIE 9474, Signal Processing, Sensor/Information Fusion, and Target Recognition XXIV*, volume 9474, page 94740P. SPIE, 2015. doi: 10.1117/12.2177653.

- Dominik Nuss, Stephan Reuter, Markus Thom, Ting Yuan, Gunther Krehl, Michael Maile, Axel Gern, and Klaus Dietmayer. A random finite set approach for dynamic occupancy grid maps with real-time application. *The International Journal of Robotics Research*, 37(8):841–866, 2018. doi: 10.1177/0278364918775523.
- Jakub Porebski. Customizable inverse sensor model for Bayesian and Dempster-Shafer occupancy grid frameworks. In *Advanced, Contemporary Control*, volume 1196 of *Advances in Intelligent Systems and Computing*, pages 1225–1236. Springer International Publishing, 2020. doi: 10.1007/978-3-030-50936-1_102.
- Sven Richter, Yiqun Wang, Johannes Beck, Sascha Wirges, and Christoph Stiller. Semantic evidential grid mapping using monocular and stereo cameras. *Sensors*, 21(10):3380, 2021. doi: 10.3390/s21103380.
- Donald J Schuirmann. A comparison of the two one-sided tests procedure and the power approach for assessing the equivalence of average bioavailability. *Journal of Pharmacokinetics and Biopharmaceutics*, 15(6):657–680, 1987. doi: 10.1007/BF01068419.
- Glenn Shafer. *A Mathematical Theory of Evidence*. Princeton University Press, Princeton, NJ, 1976.
- Florentin Smarandache and Jean Dezert. Proportional conflict redistribution rules for information fusion. In *Advances and Applications of DSMT for Information Fusion*, volume 2, pages 3–68. American Research Press, 2006.
- Philippe Smets. Decision making in the tbm: the necessity of the pignistic transformation. *International Journal of Approximate Reasoning*, 38(2):133–147, 2005. doi: 10.1016/j.ijar.2004.05.003.
- Philippe Smets and Robert Kennes. The transferable belief model. *Artificial Intelligence*, 66(2):191–234, 1994. doi: 10.1016/0004-3702(94)90026-4.
- Cyrill Stachniss. Freiburg building 079 dataset. University of Freiburg, Department of Computer Science, 2003. Available at <https://dspace.mit.edu/handle/1721.1/62290>.
- Sebastian Thrun, Wolfram Burgard, and Dieter Fox. *Probabilistic Robotics*. MIT Press, 2005.
- Ronald R Yager. On the Dempster-Shafer framework and new combination rules. *Information Sciences*, 41(2):93–137, 1987. doi: 10.1016/0020-0255(87)90007-7.
- Lotfi A Zadeh. On the validity of Dempster’s rule of combination of evidence. Technical Report UCB/ERL M79/24, Electronics Research Laboratory, University of California, Berkeley, 1979.

Supplementary Material: Equivalence and Divergence of Bayesian Log-Odds and Dempster’s Combination Rule for 2D Occupancy Grids

Tatiana Berlenko, Kirill Krinkin

S1 Statistical Methodology

This supplement presents the complete statistical analysis framework summarized in the main text.

S1.1 Directional Analysis

As a distribution-free primary measure of effect reliability, we report k/N : the number of runs in which the Bayesian arm achieves a higher (or lower, for Brier score and entropy) metric value than the belief function arm. This sign-test-like statistic requires no assumptions about effect size distributions and is robust to outliers.

S1.2 Equivalence Testing (TOST)

We apply the Two One-Sided Tests (TOST) procedure [Schuirmann \[1987\]](#), [Lakens \[2017\]](#) to assess whether performance differences fall within practically negligible bounds. TOST rejects the null hypothesis of non-equivalence when the $(1 - 2\alpha)$ confidence interval for the mean paired difference $\bar{d} = \overline{x - y}$ falls entirely within $(-\delta, +\delta)$, where δ is the equivalence margin.

Rather than reporting equivalence at a single pre-specified margin, we present a **sensitivity analysis** as the primary TOST result: for each metric-condition pair, we sweep the margin from $0.5\times$ to $2\times$ the nominal value and report the smallest margin at which equivalence holds and the breakpoint at which it fails. This approach provides strictly more information than a single-margin test and avoids dependence on a potentially arbitrary margin choice.

As secondary support, we provide a practical argument for the nominal margins: at 0.1 m grid resolution, a cell accuracy margin of $\delta = 0.02$ corresponds to approximately 2 misclassified cells per 100 observed cells, which is negligible for downstream path planning and obstacle avoidance at standard navigation tolerances.

S1.3 Effect Sizes

Paired Cohen’s d is computed as $d = \bar{d}/s_d$, where s_d is the standard deviation of the paired differences. Confidence intervals use the Hedges–Olkin [Hedges and Olkin \[1985\]](#) variance approximation:

$$\widehat{\text{Var}}(d) = \frac{1}{n} + \frac{d^2}{2(n-1)}, \quad (\text{S1})$$

with 95% CIs constructed via $d \pm t_{0.975, n-1} \cdot \sqrt{\widehat{\text{Var}}(d)}$.

For verification, we also compute exact confidence intervals via non-central t distribution inversion [Steiger \[2004\]](#): for each observed t -statistic, the non-centrality parameters δ_{lo} and δ_{hi} satisfying $P(T > t_{\text{obs}} \mid \delta_{\text{lo}}) = \alpha/2$ and $P(T < t_{\text{obs}} \mid \delta_{\text{hi}}) = \alpha/2$ are found numerically, yielding exact CI bounds $d = \delta/\sqrt{n}$. Across all nine comparisons, the maximum absolute discrepancy

between the Hedges–Olkin and non-central t CI bounds is 0.59, which is less than 4% of the corresponding point estimate. All qualitative conclusions are identical under both methods.

Interpreting large d values Cohen’s Cohen [1988] benchmarks ($d = 0.2$ small, 0.5 medium, 0.8 large) were calibrated for human behavioral studies with high individual variability. In computational experiments with controlled environments and fixed random seeds, within-run variance approaches zero as the simulation becomes more deterministic, inflating d without limit. The effect sizes reported in this study ($d = 4.6$ to 14.9) reflect very low within-method variance (standard deviation of paired differences $s_d = 0.0001$ – 0.012), not large absolute differences. The raw mean differences are 0.001–0.070 on $[0, 1]$ scales. We report both raw differences and d values throughout, and note that the k/N directional consistency provides a more intuitive measure of effect reliability in this setting.

S1.4 Multiplicity Correction

The nine simulation TOST comparisons (3 metrics \times 3 conditions: single-agent, dynamic baseline, noisy sensor) are corrected as a single family using the Holm–Bonferroni step-down procedure Holm [1979], which controls the family-wise error rate while being uniformly more powerful than the Bonferroni correction. This is a conservative choice: correcting per-experiment (family size 3) yields identical conclusions for all comparisons.

S1.5 Real-Data Statistical Analysis

The real-data experiments (Intel Lab, Freiburg 079) produce a single map per condition rather than independent replications. We therefore use a *spatial block bootstrap* to construct 95% confidence intervals that account for spatial autocorrelation in occupancy grids.

The grid is partitioned into non-overlapping $B \times B$ cell blocks (default $B = 10$ cells = 1.0 m at 0.1 m resolution). For each metric, only blocks containing at least one evaluation cell are retained. At each of 10,000 bootstrap iterations, blocks are resampled with replacement; the per-cell metric differences from all cells in the resampled blocks are aggregated to compute the mean delta. The 95% percentile CI is then extracted from the bootstrap distribution.

The block size of 1.0 m is chosen to exceed the grid cell size by a factor of $10\times$, capturing local spatial dependence from overlapping lidar rays. The autocorrelation range is expected to be less than 2.0 m for indoor lidar grids at 0.1 m resolution, based on the beam footprint (0.1–0.5 m at typical indoor ranges) and the resulting local correlation structure. A sensitivity analysis over block sizes $B \in \{5, 10, 20\}$ (0.5 m, 1.0 m, 2.0 m) confirms that CI widths and significance verdicts are stable across this range (section S1.8).

S1.6 Bayes Factors

As a complementary Bayesian measure, we compute BF_{01} for each comparison using a conjugate normal model with a weakly informative prior $\mu_d \sim \mathcal{N}(0, \delta^2)$ centered at zero with scale equal to the equivalence margin. $\text{BF}_{01} > 1$ favors equivalence; values exceeding 10^6 indicate overwhelming posterior concentration within the equivalence region.

Bayesian equivalence testing yields $\text{BF}_{01} > 10^6$ for all five TOST-equivalent comparisons, indicating overwhelming posterior concentration within the equivalence region. The four non-equivalent comparisons yield $\text{BF}_{01} \approx 0$, indicating strong evidence against equivalence. The BF results are fully consistent with the frequentist TOST verdicts. The prior scale equals the TOST margin, coupling the two analyses; however, the overwhelming magnitude of $\text{BF}_{01} (> 10^6)$ ensures robustness to any reasonable prior specification.

S1.7 CI Verification

Table S1 reports the verification of Cohen’s d confidence intervals: the Hedges–Olkin approximation Hedges and Olkin [1985] used in Table 2 of the main paper is compared against exact non-central t distribution CIs Steiger [2004] for all nine simulation comparisons. The maximum absolute discrepancy is 0.59, occurring for the single-agent Brier score comparison ($d = -14.93$, the largest effect size; less than 4% of the point estimate). All qualitative conclusions are identical under both methods.

Table S1: Cohen’s d CI verification: Hedges–Olkin (1985) approximation vs. exact non-central t inversion (Steiger, 2004). Maximum discrepancy is 0.59, confirming qualitative conclusions are unaffected.

Experiment	Metric	d	HO 95% CI	NCT 95% CI	Disc.
Single-agent	Cell Accuracy	+13.51	[+8.01, +19.02]	[+8.54, +18.48]	0.54
	Boundary Sharpness	+7.78	[+4.58, +10.98]	[+4.88, +10.67]	0.31
	Brier Score	-14.93	[-21.00, -8.85]	[-20.41, -9.44]	0.59
Multi-robot (dyn.)	Cell Accuracy	+6.14	[+3.59, +8.69]	[+3.83, +8.44]	0.25
	Boundary Sharpness	+5.96	[+3.48, +8.44]	[+3.71, +8.19]	0.24
	Map Entropy	-7.11	[-10.04, -4.17]	[-9.75, -4.45]	0.29
Multi-robot (noisy)	Cell Accuracy	+6.03	[+3.52, +8.53]	[+3.76, +8.29]	0.25
	Boundary Sharpness	+4.62	[+2.67, +6.57]	[+2.85, +6.38]	0.19
	Map Entropy	-6.32	[-8.94, -3.70]	[-8.69, -3.95]	0.26

S1.8 Block Size Sensitivity for Spatial Block Bootstrap

Table S2 reports CIs at $B \in \{5, 10, 20\}$ (0.5 m, 1.0 m, 2.0 m) for both real-data datasets. All significance verdicts are stable across block sizes: no comparison changes from significant to non-significant or vice versa.

Table S2: Block size sensitivity for spatial block bootstrap CIs. Each cell shows the 95% CI for the metric delta (Bayesian – Dempster). All significance verdicts are stable across block sizes.

Dataset	Setup	Metric	$B=5$ (0.5 m)	$B=10$ (1.0 m)	$B=20$ (2.0 m)
Intel Lab	1-source	Cell Accuracy	[+0.014, +0.021]	[+0.014, +0.022]	[+0.013, +0.023]
		Boundary Sharpness	[-0.006, +0.007]	[-0.007, +0.007]	[-0.007, +0.007]
		Brier Score	[-0.016, -0.010]	[-0.016, -0.010]	[-0.016, -0.009]
	2-way split	Cell Accuracy	[+0.018, +0.024]	[+0.017, +0.025]	[+0.017, +0.026]
		Boundary Sharpness	[-0.010, +0.003]	[-0.010, +0.003]	[-0.011, +0.004]
		Brier Score	[-0.018, -0.014]	[-0.019, -0.013]	[-0.020, -0.013]
	4-way split	Cell Accuracy	[+0.020, +0.025]	[+0.019, +0.026]	[+0.018, +0.027]
		Boundary Sharpness	[-0.012, +0.001]	[-0.013, +0.002]	[-0.013, +0.003]
		Brier Score	[-0.019, -0.015]	[-0.020, -0.014]	[-0.021, -0.014]
Freiburg 079	1-source	Cell Accuracy	[+0.005, +0.009]	[+0.005, +0.009]	[+0.005, +0.009]
		Boundary Sharpness	[+0.005, +0.018]	[+0.005, +0.018]	[+0.005, +0.018]
		Brier Score	[-0.009, -0.006]	[-0.009, -0.005]	[-0.009, -0.005]
	2-way split	Cell Accuracy	[+0.005, +0.009]	[+0.005, +0.009]	[+0.005, +0.010]
		Boundary Sharpness	[+0.005, +0.016]	[+0.005, +0.016]	[+0.005, +0.016]
		Brier Score	[-0.009, -0.006]	[-0.009, -0.006]	[-0.010, -0.005]
	4-way split	Cell Accuracy	[+0.005, +0.009]	[+0.005, +0.009]	[+0.005, +0.010]
		Boundary Sharpness	[+0.004, +0.016]	[+0.004, +0.016]	[+0.004, +0.016]
		Brier Score	[-0.009, -0.006]	[-0.009, -0.005]	[-0.009, -0.005]

Table S3: Convergence comparison for N identical occupied observations ($l_{\text{occ}} = 2.0$, $L_{\text{max}} = 10$, $a = 0.7616$). At $N = 1$ the methods are identical by construction (pignistic matching). The Bayesian clamp saturates at $N = 5$; Dempster–Shafer overtakes at $N \approx 7$.

N	L	$p(O)$	m_O	m_{OF}	BetP(O)	BetP $- p$
1	2.0	0.8808	0.7616	0.2384	0.8808	+0.0000
2	4.0	0.9820	0.9432	0.0568	0.9716	-0.0104
5	10.0	0.999955	0.9992	0.0008	0.9996	-0.0003
10	10.0	0.999955	≈ 1	$< 10^{-6}$	≈ 1	+0.00005
20	10.0	0.999955	≈ 1	$< 10^{-12}$	≈ 1	+0.00005

S2 Supporting Proofs

S2.1 Proof of Closed-Form Accumulation Lemma

Under the conditions stated in the main text (vacuous prior, N identical consonant occupied observations with $m_{\text{obs}} = (a, 0, 1 - a)$):

Proof. By induction on N . The base case $N = 1$ is immediate from the vacuous identity property. For the inductive step, assume $m_O^{(N)} = 1 - (1 - a)^N$ and $m_{OF}^{(N)} = (1 - a)^N$ hold at step N . Since $m_F^{(N)} = 0$ and $m_{F,\text{obs}} = 0$, the conflict is $K = 0$. Applying Dempster’s combination:

$$\begin{aligned} m_O^{(N+1)} &= m_O^{(N)} \cdot a + m_O^{(N)} \cdot (1 - a) + (1 - a)^N \cdot a \\ &= m_O^{(N)} + a(1 - a)^N \\ &= 1 - (1 - a)^N + a(1 - a)^N = 1 - (1 - a)^{N+1}. \end{aligned}$$

Similarly, $m_{OF}^{(N+1)} = (1 - a)^N \cdot (1 - a)/1 = (1 - a)^{N+1}$. □

S2.2 Multi-Observation Divergence

The single-observation equivalence holds at each individual sensor reading. Under repeated observations, the two accumulation mechanisms diverge:

- **Bayesian:** log-odds accumulate additively and are clamped at $|L| \leq L_{\text{max}}$, yielding $L^{(N)} = \min(N \cdot l_{\text{occ}}, L_{\text{max}})$ for identical occupied observations.
- **Dempster–Shafer:** masses combine multiplicatively, with conflict normalization by $1/(1 - K)$ when observations disagree.

The divergence arises from two distinct sources: (a) the Bayesian clamp imposes an artificial ceiling on confidence, while Dempster’s rule converges asymptotically to certainty without bound; and (b) Dempster’s conflict normalization factor $1/(1 - K)$ redistributes mass in a manner that has no Bayesian analogue.

S3 Convergence Analysis

Table S3 compares the two accumulation trajectories for N identical occupied observations.

The methods agree at $N = 1$ (by construction) and then diverge: Bayesian leads at $N = 2$ –5 due to faster initial accumulation, clamps at $N = 5$, and is overtaken by the Dempster–Shafer trajectory at approximately $N = 7$.

Table S4: L_{\max} ablation: Bayesian+count minus Dempster delta (15 runs each). Higher is better for cell accuracy and boundary sharpness; lower (more negative) is better for Brier score.

Metric	$L_{\max} = 5$	$L_{\max} = 10$	$L_{\max} = 20$	$L_{\max} = \infty$	Consist.
Cell accuracy	+0.0013	+0.0013	+0.0013	+0.0013	15/15
Boundary sharpness	+0.007	+0.010	+0.010	+0.010	15/15
Brier score	-0.006	-0.006	-0.006	-0.006	15/15

S4 Ablation Studies

S4.1 L_{\max} Ablation

We repeat the single-agent experiment at four clamping levels: $L_{\max} \in \{5, 10, 20, \infty\}$, with 15 runs per configuration.

The Bayesian advantage does not disappear at $L_{\max} = \infty$: the gap persists with 15/15 directional consistency for all metrics. Cell accuracy Δ is invariant (+0.0013) because it is measured at the $p = 0.5$ classification threshold, far from the saturation regime. Boundary sharpness Δ increases slightly from +0.007 ($L_{\max} = 5$) to +0.010 ($L_{\max} = \infty$).

S4.2 Yager’s Rule Comparison

Yager’s combination rule Yager [1987] assigns conflict mass to total ignorance (m_{OF}) rather than normalizing it away. In simulation, Yager performs worse than Dempster on boundary sharpness (−24% to −31% relative) because conflict-to-ignorance transfer preserves excessive uncertainty at boundary cells. Yager slightly outperforms Dempster on cell accuracy (+0.025%) but performs worse on Brier score.

On Intel Lab data, Yager shows better Brier score than Bayesian in the 1-source condition, and better cell accuracy than Dempster in scan-split configurations. However, Yager consistently produces the lowest boundary sharpness of all four arms.

S4.3 DS Regularization Control

We introduce a minimum ignorance mass floor $m_{OF,\min}$ for Dempster’s rule and test $m_{OF,\min} \in \{0.001, 0.01, 0.05\}$.

The regularization does not close the gap. On cell accuracy, the gap narrows modestly at $m_{OF,\min} = 0.05$ (6.9% reduction). On boundary sharpness, the gap *widens*: at $m_{OF,\min} = 0.05$, the disadvantage more than doubles (−116% change).

We note that $m_{OF,\min}$ is one possible DS regularization but not necessarily the closest functional analog of L_{\max} clamping. However, combined with the $L_{\max} = \infty$ ablation, the evidence supports a non-regularization explanation.

S4.4 Sensor Parameter Sensitivity

We test four sensor parameterizations: weak ($l_{\text{occ}} = 1.0$, $l_{\text{free}} = -0.3$), default ($l_{\text{occ}} = 2.0$, $l_{\text{free}} = -0.5$), strong ($l_{\text{occ}} = 4.0$, $l_{\text{free}} = -1.0$), and symmetric ($l_{\text{occ}} = 1.5$, $l_{\text{free}} = -1.5$). Each configuration uses pignistic-transform-matched masses.

The Bayesian advantage is consistent across all four configurations. Cell accuracy advantage ranges from +0.007% (symmetric) to +0.21% (strong). Boundary sharpness advantage ranges from +0.2% (symmetric) to +1.1% (weak). The advantage is smallest for the symmetric sensor ($|l_{\text{occ}}| = |l_{\text{free}}|$).

S5 Prior-Work Detailed Comparison

In the credibilist grid literature [Moras et al. \[2011b,a\]](#), the Bayesian log-odds parameters (l_{occ} , l_{free}) and the belief function masses (m_O , m_F , m_{OF}) are set by the practitioner for each framework separately. When these parameters are not formally linked, differences in the *aggressiveness* of the per-observation update can dominate the comparison, masking or even reversing the effect of the fusion rule itself.

The vinySLAM comparison with tinySLAM [Huletski et al. \[2017\]](#) illustrates a related confound: the TBM cell model and scan matching cost function were changed simultaneously without ablation. The reported accuracy improvement cannot be attributed to the belief function representation alone.

Nuss et al. [Nuss et al. \[2018\]](#) compared their RFS-based evidential grid against a standard Bayesian baseline, but the comparison employed different observation models for each framework.

The common pattern is the absence of a formal matching criterion that ensures identical per-observation decision probabilities.

References

- Jacob Cohen. *Statistical Power Analysis for the Behavioral Sciences*. Lawrence Erlbaum Associates, 2 edition, 1988.
- Larry V Hedges and Ingram Olkin. *Statistical Methods for Meta-Analysis*. Academic Press, 1985.
- Sture Holm. A simple sequentially rejective multiple test procedure. *Scandinavian Journal of Statistics*, 6(2):65–70, 1979.
- Arthur Huletski, Dmitriy Kartashov, and Kirill Krinkin. VinySLAM: An indoor SLAM method for low-cost platforms based on the Transferable Belief Model. In *2017 IEEE/RSJ International Conference on Intelligent Robots and Systems (IROS)*, pages 6770–6776. IEEE, 2017. doi: 10.1109/IROS.2017.8206595.
- Daniel Lakens. Equivalence tests: A practical primer for t tests, correlations, and meta-analyses. *Social Psychological and Personality Science*, 8(4):355–362, 2017. doi: 10.1177/1948550617697177.
- Julien Moras, Véronique Cherfaoui, and Philippe Bonnifait. Credibilist occupancy grids for vehicle perception in dynamic environments. In *2011 IEEE International Conference on Robotics and Automation (ICRA)*, pages 84–89. IEEE, 2011a. doi: 10.1109/ICRA.2011.5980298.
- Julien Moras, Véronique Cherfaoui, and Philippe Bonnifait. Moving objects detection by conflict analysis in evidential grids. In *2011 IEEE Intelligent Vehicles Symposium (IV)*, pages 1122–1127. IEEE, 2011b. doi: 10.1109/IVS.2011.5940561.
- Dominik Nuss, Stephan Reuter, Markus Thom, Ting Yuan, Gunther Krehl, Michael Maile, Axel Gern, and Klaus Dietmayer. A random finite set approach for dynamic occupancy grid maps with real-time application. *The International Journal of Robotics Research*, 37(8):841–866, 2018. doi: 10.1177/0278364918775523.
- Donald J Schuirmann. A comparison of the two one-sided tests procedure and the power approach for assessing the equivalence of average bioavailability. *Journal of Pharmacokinetics and Biopharmaceutics*, 15(6):657–680, 1987. doi: 10.1007/BF01068419.
- James H Steiger. Beyond the F test: Effect size confidence intervals and tests of close fit in the analysis of variance and contrast analysis. *Psychological Methods*, 9(2):164–182, 2004. doi: 10.1037/1082-989X.9.2.164.

Ronald R Yager. On the Dempster-Shafer framework and new combination rules. *Information Sciences*, 41(2):93–137, 1987. doi: 10.1016/0020-0255(87)90007-7.